



UNIVERSITAT POLITÈCNICA
DE CATALUNYA
BARCELONATECH



MASTER THESIS

Consistency of different tropospheric models and mapping functions for precise GNSS processing

Victoria Graffigna

SUPERVISED BY

Manuel Hernández-Pajares

Universitat Politècnica de Catalunya
Master in Aerospace Science & Technology
February 2017

This Page Intentionally Left Blank

Consistency of different tropospheric models and mapping functions for precise GNSS processing

BY

Victoria Graffigna

DIPLOMA THESIS FOR DEGREE

Master in Aerospace Science and Technology

AT

Universitat Politècnica de Catalunya

SUPERVISED BY:

Manuel Hernández-Pajares
Department of Mathematics IV

Abstract

The TOMographic Model of the IONospheric electron content (TOMION) software implements a simultaneous precise geodetic and ionospheric modeling, which can be used to test new approaches for real-time precise GNSS modeling (positioning, ionospheric and tropospheric delays, clock errors, among others).

In this work, the software is used to estimate the Zenith Tropospheric Delay (ZTD) emulating real time and its performance is evaluated through a comparative analysis with a built-in GIPSY estimation and IGS final troposphere product, exemplified in a two-day experiment performed in East Australia. In addition, the troposphere mapping function was upgraded from Niell to Vienna approach. On a first scenario, only forward processing was activated and the coordinates of the Wide Area GNSS network (relative) were loosely constrained, without fixing the carrier phase ambiguities, for both reference and rover receivers and the ionospheric modeling was turned off. On a second one, precise point positioning (PPP) was implemented, every 900 seconds, introducing IGS transmitted orbits and clocks.

Comparisons between TOMION and GIPSY estimates and IGS final product have been performed and the agreement between the the first two ones was of $\pm 5\text{mm}$, while both were over 2cm biased with respect to IGS products, despite using IGS satellite clocks and orbits for TOMION computations. Moreover, the standard deviation of the TOMIONs estimates computed in PPP mode was between 3 and 13mm, when compared to both external references. Additionally, Vienna mapping function showed in general a fairly better agreement than Niell although further improvement could be achieved for such estimations with coefficients for the Vienna mapping function calculated from raytracing as well as integrating meteorological comparative parameters.

Acknowledgments

This work is based on the functioning of a software developed by Manuel Hernández Pajares, to whom I am very grateful for the countless hours he devoted to explaining and expertly guiding me throughout this discovery. His unwavering enthusiasm kept me constantly engaged to this research.

My appreciations also extends to my former and future colleagues in La Plata. Mauricio Gende's mentoring and encouraging have been specially valuable and his early faith put on me since 2007 while I was his undergraduate student. Thanks also to Claudio Brunini, who was the essential link that brought me to IonSAT group.

I would also like to thank to Julieta and Belen, who have been my support and we have developed a real true friendship and we have grown up together in this adventure. And to the volleyball team that have been an excellent time off from the books. And finally, I would like to thank to the many people that I have left behind, but have always had them close: Ale, my parents, my sister, and my closest friends Nati, Coti, Mari, Ivi, Nanu, Facu, Dedu, Lu, Santi, Gabo, Mica, Lau, Pani... They have all accompanied me in the distance and they have travel to visit me and, the most important, are happily waiting for my return.

For you, my love,
for one of the first
of many realizations
that we are to share...

CONTENTS

CHAPTER 1. INTRODUCTION	1
1.1. Context	1
1.2. Troposphere Modelling	1
1.2.1. Zenith Hydrostatic Delay	2
1.2.2. Zenith Wet Delay	3
1.2.3. Troposphere Mapping functions	3
 CHAPTER 2. DATA AND EXPERIMENTS	 11
2.1. The Network	11
2.2. TOMION	11
2.2.1. Introduction	11
2.2.2. Overview: Description of the software	13
2.2.3. Observables	14
2.2.4. Modeling the observables	14
2.2.5. Prefit	16
2.2.6. Filter	18
2.2.7. Processing strategy	21
2.2.8. Ambiguity resolution	26
2.2.9. TOMION's Mapping Functions	28
2.3. External sources	31
2.3.1. GIPSY	31
2.3.2. IGS	32
 CHAPTER 3. RESULTS	 33
3.1. Introduction	33
3.2. First Computations	33
3.2.1. Process Noise	34
3.2.2. The tropospheric delay as a quality factor	35
3.2.3. Filtering the outliers	35
3.3. The new mapping function	37
3.4. Zenith Troposphere Delay	39
3.4.1. Relative	39

3.4.2. PPP	43
3.5. Summary of results	46
CONCLUSIONS	49
Bibliography	51
APPENDIX A. Appendix	57
A.1. Coefficients for Niell Mapping Function	57
A.2. Combinations of measurements	57
A.3. Zenith Tropospheric Delay in WARTK mode for Niell Mapping Function	59
A.4. Statistics of the comparison between the mapping functions in Precise Point Positioning	60

LIST OF FIGURES

1.1 Bending of the ray in the neutral atmosphere	2
1.2 Sensitivities of the different mapping functions.	7
2.1 The Network.	12
2.2 TOMION's Processing Concept.	13
2.3 Pseudorange measurement contents.	15
2.4 Linearization of the distance between satellite and receiver.	17
2.5 Principle of Kalman filtering.	20
2.6 Basic concept of relative positioning.	23
2.7 Bilinear interpolation.	28
2.8 TOMION's mapping functions.	30
3.1 First computations of ZTD	34
3.2 The troposphere delay as a quality factor.	35
3.3 Statistics Relative (Niell) w.r.t IGS for <i>before</i> and <i>after</i> removing the outliers.	36
3.4 Statistics Relative w.r.t IGS for Niell and Vienna mapping functions	38
3.5 Visibility from reference station <i>tidb</i>	40
3.6 ZTD computed in WARTK (Vienna) mode with TOMION, with GIPSY and IGS final product.	41
3.7 Statistics Relative w.r.t GIPSY for Niell and Vienna mapping functions	42
3.8 Zenith Troposphere Delay in PPP.	44
3.9 Statistics PPP w.r.t. GIPSY for Niell and Vienna mapping functions	45
3.10BIAS of ZTD in PPP and in WARTK strategies, for Niell and Vienna mapping functions w.r.t GIPSY and IGS.	47
3.11SD of ZTD in PPP and in WARTK strategies, for Niell and Vienna mapping functions w.r.t GIPSY and IGS.	48
3.12RMS of ZTD in PPP and in WARTK strategies, for Niell and Vienna mapping functions w.r.t GIPSY and IGS	48
A.1 ZTD computed in WARTK (Niell) mode with TOMION, with GIPSY and IGS final product.	59
A.2 Statistics PPP w.r.t IGS for Niell and Vienna mapping functions	60
A.3 Statistics PPP w.r.t GIPSY for Niell and Vienna mapping functions	61

LIST OF TABLES

1.1	Refractivity Formula Constants.	3
1.2	Input Parameters for Hydrostatic and Wet Mapping Functions of NMF and VMF. . . .	7
1.3	Comparison between GMF, GPT2 and GPT2w.	9
2.1	Station Elipsoidal Coordinates	12
2.2	Relative Positioning vs. Precise Point Positioning	26
3.1	Statistics WARKT Niell w.r.t. IGS <i>before</i> removing filter postfit outliers.	37
3.2	Statistics WARKT Niell w.r.t. IGS <i>after</i> removing filter postfit outliers.	37
3.3	Statistics WARKT Vienna w.r.t. IGS.	38
3.4	Observations for each station for the studied interval.	39
3.5	Baselines lengths.	40
3.6	Statistics WARKT Niell w.r.t GIPSY	42
3.7	Statistics WARKT Vienna w.r.t GIPSY	43
3.8	Statistics PPP Vienna w.r.t. GIPSY	45
3.9	Statistics PPP Niell w.r.t. GIPSY	46
A.1	Coefficients of the Niell hydrostatic mapping function.	57
A.2	Coefficients of the Niell wet mapping function.	57

Chapter 1

INTRODUCTION

1.1. Context

Troposphere Delay is one of the main error sources in the analysis of space geodetic techniques operating at microwave frequencies, such as Global Navigation Satellite Systems (GNSS). The greatest effort has been put in the last 20 to 25 years in obtaining a sufficiently exact model for this deterioration in the signal, mostly to be able to decorrelate it from the site's coordinates, especially the vertical.

The limiting error in the accuracy of the estimated geodetic parameters for geodetic applications, for which observations are sometimes made to low elevation angles (below 10°), is thought to be the indeterminacy of the mapping functions, including departures of its coefficients from a realistic representation, for both the hydrostatic and wet components. Throughout this work, the performance of different mapping functions is studied and evaluated in an in-house software named TOMION within several experiments, as well as comparisons with external sources.

Over the last few years, the need for instantaneously precise positioning from several currently on going applications has set the sights onto *empirical* global mapping functions where its parameters are tabulated and can fairly easily be interpolated for a given site. We will also dedicate some of the the contents of the study to applying the modern approach to TOMION.

Background to this study rely on a presentation on the Workshop on Space Geodesy and Ionospheric Research (SGI) performed in Berlin in August 2016 [Graffigna et al., 2016], where the first computations related to this study were lectured. Recently, the research has been admitted to the EGU (European Geosciences Union) General Assembly 2017 in the Atmospheric Remote Sensing with Space Geodetic Techniques Session [Graffigna et al., 2017b] and also it has been submitted to the AAGG (Argentine Geodesy and Geophysics Association) meeting taking place this year as well, in April [Graffigna et al., 2017a].

1.2. Troposphere Modelling

The neutral refractivity along the ray path is not easily or economically measured, therefore the delay must in general be calculated or estimated. The delay is conveniently divided into two components, which have been designated the hydrostatic and wet components of the atmosphere delay, and the line of sight delay for each component is modeled as the product of the zenith delay and a geometric factor, the *mapping function*, which describes the elevation angle dependence of the delay.

For practical purposes, azimuthal symmetry is generally assumed; so it will be here. If ε is

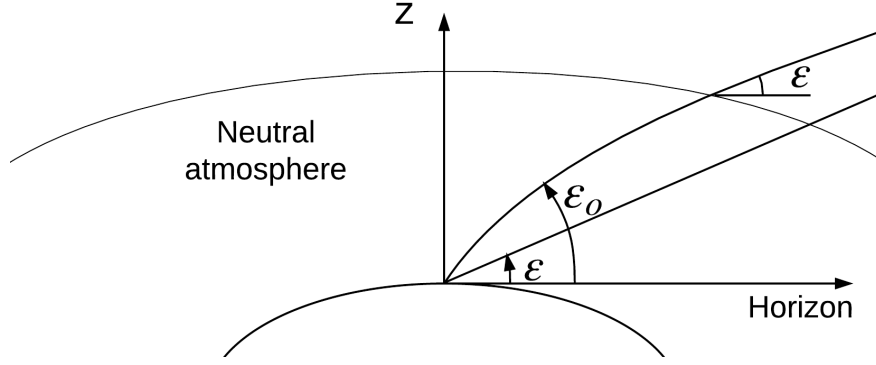


Figure 1.1: Bending of the ray in the neutral atmosphere. The outgoing (vacuum) elevation angle ϵ is smaller than the initial elevation angle ϵ_0 .

the elevation angle, then we have ¹:

$$\Delta\rho_{trop} = \Delta\rho_d^z m_d(\epsilon) + \Delta\rho_w^z m_w(\epsilon), \quad (1.1)$$

where by the superscript z we denote the zenith path; by the subscripts d and w the dry or wet components; by m the mapping functions; and by $\Delta\rho$ a path delay.

The geometric bending effect refers to the actual longer distance that the signal travels due to its refraction in the medium different to the vacuum, as it can be seen in figure 1.1. This additional apparent time is accounted for in the hydrostatic component.

1.2.1. Zenith Hydrostatic Delay

Saastamoinen [1972] showed that the delay in the zenith direction due to the atmospheric constituents in hydrostatic equilibrium is accurately determined by measuring the surface pressure and making corrections for the latitude and height above sea level of the site from which the observation is being made. His formula (or the slightly more precise form given by Davis et al. [1985]) provides the zenith hydrostatic path with an accuracy of better than 1 mm under conditions of hydrostatic equilibrium:

$$\Delta\rho_d^z = 10^{-6} K_1 R_d \int_H^\infty \sigma dz, \quad (1.2)$$

$$\int_H^\infty \sigma dz = - \int_{P_s}^0 \frac{1}{g} dP = \frac{P_s}{g_m}, \quad (1.3)$$

$$\Delta\rho_d^z = 10^{-6} K_1 R_d \frac{P_s}{g_m}. \quad (1.4)$$

Knowledge of the instantaneous local pressure arises from barometric recordings, the gridded surface pressure output of a numerical weather model (NWM) or global empirical models, which approximate the spatial and temporal pressure variability.

¹ Note that there is a slight difference between the term hydrostatic and dry. The first one implies that the gases are in hydrostatic equilibrium whereas the second means all the gases except for the water vapor. However, there is only a small amount of gases that are not in hydrostatic equilibrium and at the same time are not the water vapor. Since this quantity is not significant, it is well accepted in the field that the term hydrostatic and dry are used indistinctly.

1.2.2. Zenith Wet Delay

Davis et al. [1985] derived zenith wet delay from the refractivity of the remaining gases not modeled as in hydrostatic equilibrium like:

$$\Delta p_w^z = 10^{-6} \int_H^\infty [K'_2 \frac{e}{T} + K_3 \frac{e}{T^2}] Z_w^{-1} dz. \quad (1.5)$$

Not long after, Askne and Nordius [1987] suggested to introduce:

$$T_m = \frac{\int_H^\infty \frac{e}{T} dz}{\int_H^\infty \frac{e}{T^2} dz} \quad \text{and} \quad e = e_s \left(\frac{p}{p_s} \right)^{(\Lambda+1)}, \quad (1.6)$$

so to derive the following closed formula:

$$\Delta p_w^z = 10^{-6} \left[K'_2 + \frac{K_3}{T_m} \right] \frac{R_d}{(\Lambda+1)g_m} e_s. \quad (1.7)$$

The constants $K'_2 = K_2 - K_1(R_d/R_w)$ and K_3 are empirically determined and expressed in table 1.1. R_d is the specific gas constant for the dry constituents and R_w for the wet ones². The g_m , which is the gravity acceleration at the mass center of the vertical column of the atmosphere, can be computed as a function of the locations' latitude and orthometric height H . The water vapor partial pressure at mean sea level is denoted as e_s and T_m the weighted mean temperature at height H along the local vertical.

value of K	Unit of Measure
$k_1 = 77.604 \pm 0.014$	$K/mbar$
$k_2 = 64.79 \pm 0.08$	$K/mbar$
$k_3 = (3.776 \pm 0.004) \times 10^5$	$K^2/mbar$

Table 1.1: Refractivity Formula Constants. From: [Thayer, 1974].

In essence, to use equation 1.7 for determination of the zenith wet delays, we need the water vapor pressure at the site, the weighted mean temperature, and the water vapor decrease factor Λ . While T_m can be derived from a two parameter formula ($T_m(\Lambda, \alpha)$), where α is the rate of temperature change occurring within a rising or descending air parcel; the derivation of Λ evades a straightforward treatment because it is implicitly defined by the water vapor pressure e which is highly variable with height.

1.2.3. Troposphere Mapping functions

The atmospheric mapping function does not vary simply as cosecant of the elevation ε , which would be expected for a plane-parallel refractive medium, because of the curvature of the atmosphere. Thus, the mapping functions are a measure for the thickness of the atmosphere

²The wet term includes what is not modeled by the hydrostatic equilibrium equation

compared to the Earth radius. A wide range of mapping functions has been used in the past. For example, the Niell Mapping Functions (NMF; [Niell, 1996]) and the global mapping functions (GMF; [Böhm et al., 2006]) are empirical or the so-called blind mapping functions which only need the day of year and approximate station coordinates as input. Alongside such climatological approaches, the isobaric mapping functions (IMF; [Niell, 2000]) and the Vienna mapping functions 1 (VMF1; [Boehm and Schuh, 2004]) account for the actual refractivity being derived from the operational analysis fields of numerical weather models at the epoch of the observations. Consequently, VMF1 positively exceeds NMF and GMF in terms of accuracy, but it is also prone to being inapplicable if the underlying mapping functions have not been updated.

Among the several Troposphere Mapping functions available for computations in the literature, here it will be only gone in deeper detail for the ones involved in the computations within this work and the reason of this will be summarize in section 1.2.3.3.

1.2.3.1. Niell Mapping Functions, 1996:

The strong dependence of the best mapping function, functions by Herring [1992], available at the time on surface temperature induced Niell to develop the New Mapping Functions (NMF, now often called Niell Mapping Functions). He developed expressions for calculating the ratios (mapping functions) of the line of sight hydrostatic and wet atmospheric path delays to their corresponding zenith delays at radio wavelengths for elevation angles down to 3° . The form adopted for these mapping functions is the continued fraction of Marini [1972] with three constants but normalized to unity at the zenith as by Herring [1992]. The factor in the denominator ensures that the mapping function is equal to one in the zenith direction:

$$m(\epsilon) = \frac{1 + \frac{a}{1 + \frac{b}{1 + \frac{c}{a}}}}{\sin(\epsilon) + \frac{b}{\sin(\epsilon) + c}}. \quad (1.8)$$

The coefficients of the continued fraction representation of the hydrostatic mapping function depend on the latitude and height above sea level of the observing site and on the day of the year; the dependence of the wet mapping function is only on the site latitude. Thus, they can be easily applied at stations without meteorological sensors, which often is the case for GNSS stations.

Similar to Davis et al. [1985] and Herring [1992], he used ray-tracing methods to determine the coefficients a , b , and c , of the continued fraction form in eq. 1.8. Ray traces were computed at nine elevations from 3° to 90° for each of the (coincidentally) nine sets of standard temperature and relative humidity profiles to give both the hydrostatic and wet path delays. A least squares fit to the values at the nine elevation angles was made for the three coefficients, a , b , and c , for each of the nine profiles.

He also found that the temporal variation of the hydrostatic mapping functions for the four sites that he was studying was shown to be sinusoidal within the scatter of the data. The period was found to be 365.25 days and the maximum/minimum set to January 28, the value obtained when all data were fit together, hence was adopted to define the phase of the mapping function.

Niell used standard atmosphere data at various latitudes above the equator to determine

hydrostatic and wet mapping functions down to 3° elevation. Since no data from the southern hemisphere was used in developing these mapping functions, the inversion of the seasons has been accounted for simply by adding half a year to the phase for southern latitudes.

For the hydrostatic mapping function the parameter x at tabular latitude φ_i (see Appendix A.1.) at time t from January 0.0 (in UT days) is calculated as

$$x(\varphi_i, t) = x_{avr}(\varphi_i) + x_{amp}(\varphi_i) \cos\left(\frac{2\pi(t - T_0)}{365.25}\right), \quad (1.9)$$

where x could be a , b or c and T_0 is the adopted phase, day of year (DOY) 28, as described above. The value of $x(\varphi, t)$ is obtained by interpolating linearly between the nearest $x(\varphi_i, t)$. For the wet mapping function, only an interpolation in latitude for each parameter is needed (i.e. $x_{amp}^{wet} = 0$), that means no temporal variation is considered for a fixed point.

In addition to a latitude and season dependence due to varying solar illumination, the hydrostatic Niell mapping function is also to be dependent on the height above the geoid of the point of observation because the ratio of the atmosphere "thickness" to the radius of curvature decreases with height. This does not apply to the wet mapping function since the water vapor is not in hydrostatic equilibrium, and the height distribution of the water vapor is not expected to be predictable from the station height.

The height correction is then:

$$\Delta m(\varepsilon) = \frac{dm(\varepsilon)}{dh} H, \quad (1.10)$$

where H is the height of the site above sea level in kilometers.

By comparing with mapping functions calculated from radiosonde profiles for sites at latitudes between 43°S and 75°N , the hydrostatic Niell mapping function was seen to be more accurate than, and of comparable precision to, mapping functions currently in use at the time, which were parameterized in terms of local surface meteorology. When the NMF mapping functions are used in the analysis of geodetic very long baseline interferometry (VLBI) data, the estimated lengths of baselines up to 10,400 km long change by less than 5 mm as the minimum elevation of included data is reduced from 12° to 3° . [Böhm and Schuh, 2013]

The independence of the Niell mapping functions from surface meteorology, while having comparable accuracy and precision to those that require such input, makes them particularly valuable for those situations where surface meteorology data are not available.

1.2.3.2. Vienna Mapping Functions, 2005:

The main idea for the Vienna Mapping Functions (VMF1) is to *simply* use the raytracing through the pressure level data from NWM (Numerical Weather Model), the ECMWF (European Centre for Medium-Range Weather Forecasts) in this case. [Boehm and Schuh, 2004]

The continued fraction form which is used for the hydrostatic and wet mapping function is shown in (equation 1.8). This form is also used in the NMF and in the IMF. Two approaches are introduced to derive the coefficients for the continued fraction forms of the mapping functions: whereas the 'rigorous approach' is rather time consuming, the 'fast approach' needs only one raytrace per epoch and site. As one desires to compute the delay for a rover or site that does not have a close profile measurement available, the implementation of this strategy is not realistic.

Furthermore, the computational time is not affordable for most applications although, for static and very precise requirements, it would be the very best option.

Input parameters for the raytracing program are an initial elevation angle ε_0 , sketched in figure 1.1, and values for height, temperature and water vapor pressure at 15 distinct pressure levels. The raytracing then yields the outgoing (= vacuum) elevation angle ε , and the values for the hydrostatic and the wet mapping function. The hydrostatic mapping function also includes the geometric bending effect.

For each site (e.g. VLBI station) and each epoch when ECMWF pressure level data are available, i.e. every six hours, the hydrostatic and wet mapping functions as well as the outgoing elevation angles are determined by raytracing through the pressure levels at ten different initial elevation angles (90° , 70° , 50° , 30° , 20° , 15° , 10° , 7° , 5° , 3.3°), denoted as ε_0 in figure 1.1. Then, the coefficients a , b , and c for the continued fraction forms (eq. 1.8) for the hydrostatic and wet mapping functions are estimated in a least-squares procedure. They showed that three coefficients were enough to map down the zenith delays to 3° elevation. So, at each site a time series of six parameters (a_h , b_h , c_h , a_w , b_w , c_w) exists with a resolution of six hours.

Although computers are very fast today, raytracing is still time consuming, especially if it has to be performed on a global grid, four times per day and ten times per grid point. For this reason, a fast version of the rigorous way has been developed that yields similar values for the mapping functions. Instead of determining the raytracing at ten different elevation angles, the raytracing is only calculated for one initial elevation angle of 3.3° . This yields one value for the hydrostatic, one for the wet mapping function and the vacuum elevation angle (3°). Then, predefined formulas are used for the b and c coefficients, and the coefficients a can be determined by simply inverting the continued fraction form (equation 1.8). For the hydrostatic mapping function the coefficients b_h and c_h are taken from the hydrostatic part of the isobaric mapping function IMF. If φ is the geodetic latitude, the coefficients are determined by:

$$b_h = 0.002905; \quad (1.11) \quad b_w = 0.00146; \quad (1.13)$$

$$c_h = 0.0634 + 0.0014\cos(2\varphi); \quad (1.12) \quad c_w = 0.04391. \quad (1.14)$$

1.2.3.3. The modern approach

Summarizing the previous sections, in table 1.2 is been given an overview of the input parameters for NMF and for VMF1 in both of its approaches. On one hand, we have explained that while NMF are relatively easy to implement, the same cannot be said for VMF1 in the fast determination of the coefficients nor in the most accurate, the rigorous form. However, these coefficients have been calculated for IGS and VLBI sites but for any other cite or position, this approach is not realistic. The fast approach is not as laborious as the longer one, but still requires the knowledge of vertical profiles of atmospheric parameters at the time of observation.

We will call as it is usual in the related literature, *empirical* mapping functions to those where the coefficients have been achieved by fitting NWM values to spatial and temporal variations. On the contrary, *modeled* mapping functions are the ones that take NWM values and obtain the coefficients straight for the site and epoch of the observation. This following section comes to introduce a compromise between availability of the coefficients and parameters of the most accurate mapping functions and the effort to achieve it.

In the past 10 to 15 years a lot of effort has been put on finding a higher accuracy model for

	Niell	VMF (fast)	VMF (rigorous)
<i>Hyd.</i>	doy, h, φ	a raytraced (p, h, T, e at 15 levels) for $\varepsilon_0, \varphi, \lambda, H, doy$ b and c from eqs. 1.11, 1.12	Repeat for 10 different ε_0 and for b and c
<i>Wet</i>	φ	a raytraced (p, h, T, e at 15 levels) for $\varepsilon_0, \varphi, \lambda, H, doy$ b and c from eqs. 1.13, 1.14	Repeat for 10 different ε_0 and for b and c
<i>Height Corr.</i>	Yes (in Hyd.)	Yes (in Hyd.)	No

Table 1.2: Input Parameters for Hydrostatic and Wet Mapping Functions of NMF, VMF (fast) and VMF (rigorous). Adapted from: [Boehm and Schuh, 2004]

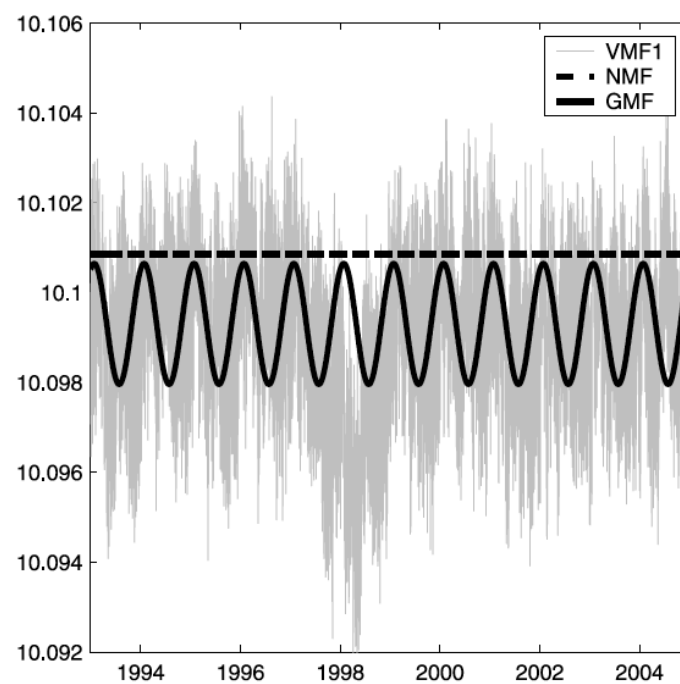


Figure 1.2: Hydrostatic mapping function at 5° elevation at Fortaleza, Brazil. Phenomena such as el Niño event in 1997 and 1998 cannot be accounted for with empirical mapping functions like NMF and GMF. Adapted from: [Böhm et al., 2006].

the troposphere delay. Some interest may arise from the quick change over space and time that the troposphere experiments. This source of error is not only very hard to model and predict for real time applications, but also for post-processing it can be an arduous job to decorrelate it from the site coordinates. Such obstacles encouraged many scientists to test several models for the tropospheric delay, as it is of our interest to have a better determination of it and improve the site coordinates precision.

It is well known in the meteorology GNSS field that the Vienna Mapping functions are one of the best candidates to project the slant delay to the zenith [Böhm et al., 2015]. For the construction of these, one needs to compute the coefficients of equation 1.8 as explained in section 1.2.3.2..

Later on, Böhm et al. [2006] introduced a new *empirical* mapping function Global Mapping Function (GMF) based on numerical weather model data. The concept happened to be somehow revolutionary in the sense that no longer instantaneous data is needed for processing.

The development of the coefficients involve an expansion in spatial spherical harmonics of the VMF1 of degree and order $n = m = 9$, leading to coarse horizontal resolution of about 20° . Hence, they have a dependance with the station coordinates; and an annual cosine variation.

The coefficients a_h and a_w for the GMF are just like the NMF ones (eq. 1.9), but the average term, the annual mean, a_0 comes as:

$$a_0 = \sum_{n=0}^9 \sum_{m=0}^n P_{mn}(\sin\varphi) [A_{mn}\cos(m\lambda) + B_{mn}\sin(m\lambda)], \quad (1.15)$$

where φ and λ are the station latitude and longitude, respectively. The P_{mn} , A_{mn} and B_{mn} are the parameters that they have adjusted by Least Square (LS) procedure for a_0 as well for the amplitude term (A), using a global grid of monthly mean profiles for pressure, temperature and humidity from the ECMWF (European Centre for Medium-Range Weather Forecasts), for the period September 1999 to August 2002. By means of the weather model, the a_h and a_w are computed thought raytracing and then by LS adjustment, the spherical harmonics are determined. All these coefficients of the values for a_0 and the annual amplitude for computing a in eq. 1.9 for each grid point are given within the function in GGOS [2017]. For the pressure and the temperature, analogous procedure is conducted as for a_0 and A . The b_h , c_h , b_w and c_w are the same as the fast form of the VMF1.

This approach can be used without introducing systematic biases in the coordinate system, although the short term precision would suffer. The GMF came to serve at the time as a back-up mapping function or a compatible empirical representation of the more complex NWM-Based mapping functions.

In Fig. 1.2 it can be seen the different sensitivities of the mentioned mapping functions. While NFM is fairly the same for the whole decade, the GMF accounts for the annual variability and VMF1 si the only one that can represent the real weather behavior. The coefficients for this study are the ones computed by raytracing for 15 different elevations, that is the rigorous form of VMF1.

The improvement of empirical models for tropospheric slant delays continued with the development of Global Pressure and Temperature (GPT2, Lagler et al. [2013]) that basically mended some of the weaknesses of GMF. The grid was reduced to 5° , the vertical resolution and temporal coverage was considerably extended from 23 to 37 isobaric levels and from annual to annual and semiannual variations in all parameters. Now, there is a *grid* that supports this computa-

	GMF	GPT2
NWM data	Monthly mean profiles from ERA-40 (23 pressure levels): 1999-2002	Monthly mean profiles from ERA-Interim (37 levels): 2001-2010
Representation	Spherical harmonics up to degree and order 9 at mean sea level	5° grid at mean ETOPO5-based heights
Temporal variability	Mean and annual terms	Mean, annual, and semi-annual terms
Phase	Fixed to January 28	Estimated
Temperature reduction	Constant lapse rate -6.5°C/km assumed	Mean, annual, and semi-annual temperature lapse rate estimated at every grid point
Pressure reduction	Exponential based on standard atmosphere	Exponential based on virtual terms of temperature at each point
Output parameters	Pressure (p), temperature (T), mapping function coefficients (a_h, a_w)	p, T , lapse rate (dT), water vapor pressure (e), a_h, a_w
	GPT2w	
NWM data	Monthly mean profiles from ERA-Interim (37 levels): 2001-2010	
Representation	1° grid at mean ETOPO5-based heights	
Temporal variability	Mean, annual, and semiannual terms, with fitted phases	
Water vapor reduction	Mean, annual, and semiannual terms of water vapor decrease factor estimated at every grid point, with fitted phases	
Temperature reduction	Mean, annual, and semiannual terms of temperature lapse rate estimated at every grid point, with fitted phases	
Pressure reduction	Exponential approach with scale heights based on grid point-wise virtual temperature values	
Output parameters	Pressure, temperature and its lapse rate, water vapor pressure and its decrease factor, hydrostatic and wet VMF mapping function coefficients	

Table 1.3: Comparison between GPT, GPT2 and GPT2w.

tions, and provides the annual means and the sine- and cosine coefficients of the annual and semiannual variations for the pressure, temperature,

The work advanced with the development of GPT2w [Böhm et al., 2015], where the effort was mainly put on reducing the grid's resolution from 5 to 1°, improving the wet delay estimation, and in densifying the data used for the parameter adjustment. In table 1.3 it is briefly summarizes the differences between the models.

Chapter 2

DATA AND EXPERIMENTS

2.1. The Network

The area chosen for this study was 7 sites in the South East of Australia as it can be seen in the map 2.1. The geodetic coordinates of the selected receivers are displayed in table 2.1. This research was initially motivated by a flight that was performed in the area, in which the observations collected by the receiver on the plane, are still being investigated in order to determine correction to improve the coordinates of the trajectory of such flight.

In navigation, with receivers on surface vehicles such as ships, cars, trains, etc., the process can be modeled by the navigation equations in a rather simply manner. But with aircraft, which can change its position much more, and much faster, both vertically and horizontally, than other types of vehicle, it is more difficult to find a good dynamic model for that delay, particularly one that is suitable for implementation in a Kalman filter solution [Colombo, 2006].

Different purpose originally encouraged this study but inherited some of the aspects such as real time treatment of the observations. Along the way, the research group found that for this to be achieved, there was the need to better estimate the Zenith Troposphere Delay on for such study.

Working with the double frequency receivers would bring a finer solution but sometimes the option of making use of it is not available, i.e. in a plane receiver, at least until the frequency L_5 is functional. In addition, if it was accessible, the time and effort involved in resolving unknown biases in such measurements can stand in the way of its benefits. Strategies for the handling of this will be briefly commented throughout this text.

As it will be described in chapter 3, the large geographic separation ranging from approximately 10 km to about 1500 km between the sites, encouraged us to test the WARTK technology in this network. And for integrity on the experiments, it was also complemented with Absolute Positioning procedures.

2.2. TOMION

2.2.1. Introduction

The TOMographic Model of the IONospheric electron content (TOMION, Fig. 2.2) is fed with global GPS data in order to compute in real time, among others, geodetic parameters, such as receiver coordinates, Zenith Troposphere Delay (ZTD), global Vertical Total Electron Content (VTEC) maps, etc.

The computation of the estimates is based on a geodetic software developed at IonSAT/UPC during the last 20 years. Although the first approaches were focused on the the development of a tomography modeling for the ionosphere, TOMION indeed acquired further features for

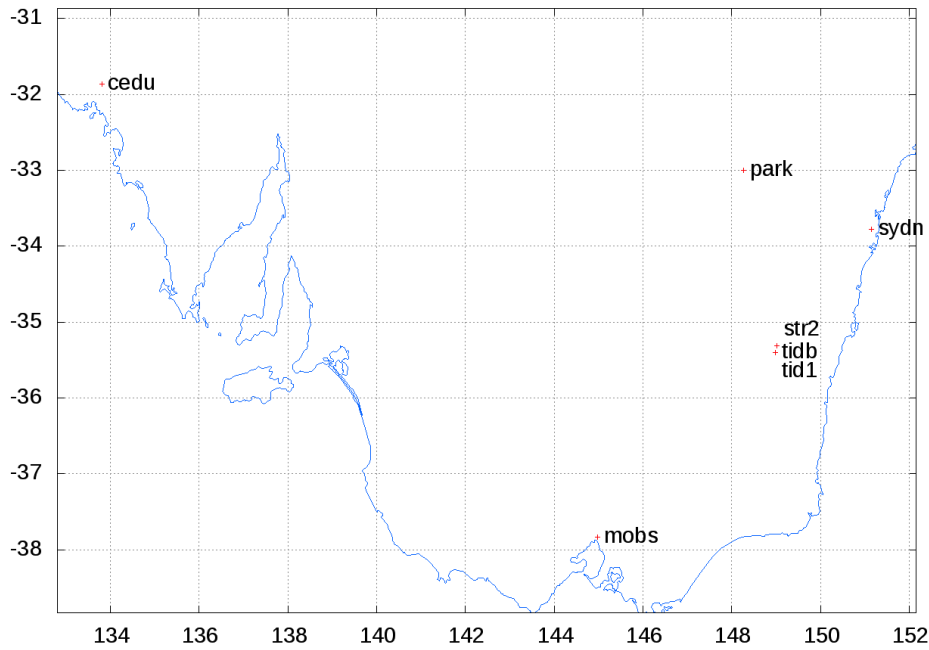


Figure 2.1: The Network.

estimating earth and atmosphere parameters.

TOMION has been built to provide several versions which are able to process ground based GNSS ionospheric data; GNSS LEO radio occultation data, [20, 15]; GNSS geodetic data, [18]; and ionosonde data, [9]. In real-time processing is also possible to provide corrections for precise user positioning (Wide Area Real-Time Kinematic (WARTK), see [16] and [33]). Since 1998, TOMION has been used in the UPC Ionospheric Analysis Centre for the IGS [19] and will be part of the analyzing committee (Galileo Reference Center) for the European Global Navigation Satellite System (Galileo) when it becomes fully operational.

In the early days of the software formulation, the ZTD was successfully estimated in differential mode (Wide Area Real-Time Kinematic (WARTK), [Hernández-Pajares et al., 2000b]). The upgrade presented here is for diverse processing modes such as PPP (Precise point positioning, sec. 2.2.7.2.) and the comparison between the strategies and higher accuracy troposphere mapping functions.

Sta. ID	Longitude (deg)	Latitude (deg)	Height (m)
cedu	133.809825000	-31.866670518	144.81717
mobs	144.975335000	-37.829411823	40.62234
park	148.264606000	-32.998772348	397.45550
str2	149.010150000	-35.316166256	802.57558
sydn	151.150375000	-33.780884170	85.67921
tid1	148.979993000	-35.399209816	665.41890
tidb	148.979996000	-35.399204806	665.36714

Table 2.1: Station Elipsoidal Coordinates

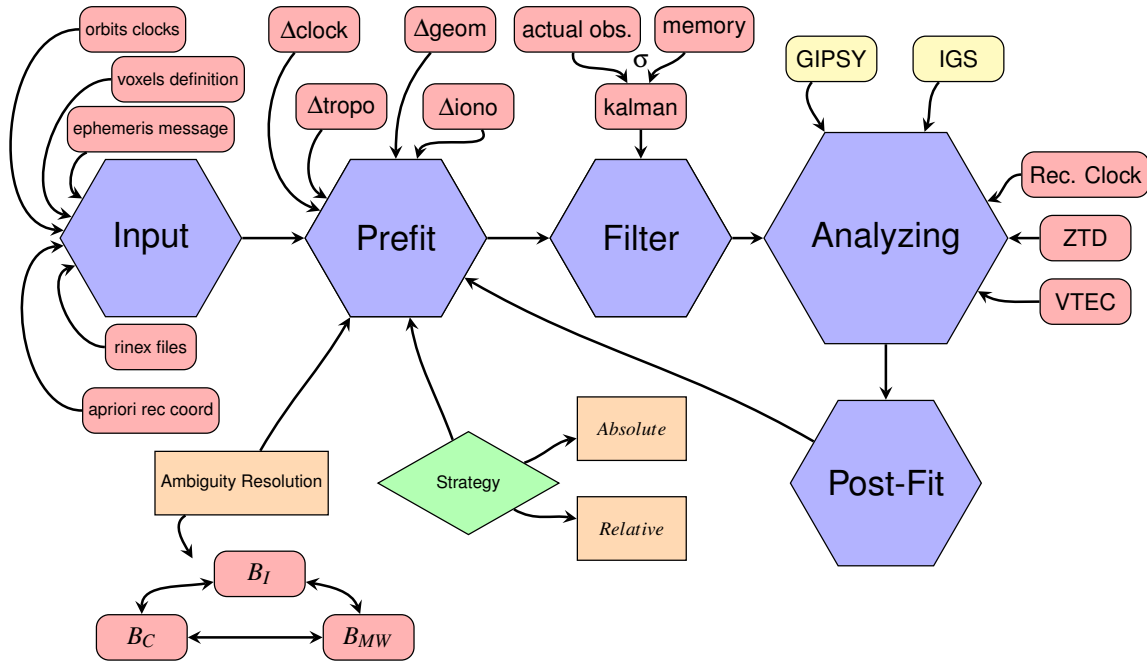


Figure 2.2: TOMION's Processing Concept.

2.2.2. Overview: Description of the software

In the GNSS processing field it is common to name the observations minus the *intended* replica of the observations, i.e. the a-priori modeled term, as *prefit*. In this chapter we will see how the software operates: The main codes that form the core of TOMION software are the ones that calculate the *prefit* and the one that computes the *filter*. As it can be seen in figure 2.2 for the *prefit*, one has all the parameters that can be modeled and subtracted from the observations, as it will be further explained in section 2.2.4.. After the *prefit*, it follows the filter which is one of Kalman's, in charged of solving the system of equation of navigation and resolving for the unknowns. For the modeling, some components are mandatory, such as the geometric a priori delay, considering the a priori receiver and the satellites' coordinates, the satellite clocks in absolute positioning, among others; while some others conjugate with the strategy used and the type of observations involved.

We will see in section 2.2.6.1., that for the Kalman filter, the user is meant to define one of the critical parameters of the computations: the process noise, denoted by σ above the module's icon on figure 2.2. This parameter will set how much the unknown is able to depart from the a priori value, and the implications of it will be seen on section ??.

The inputs to the code are automatically downloaded once the station (or network) and dates for the experiments have been defined as well as the processing strategy described in section 2.2.7.. The secondary options for the inputs are regarding the source from which the user would like to obtain the ephemeris, a priori coordinates, satellite clocks, etc.

The analyzing segment refers to generating the graphics for the parameters of interest (i.e. the ones the users selects) from the output estimations and compare them with external sources (if available). Some of them are ZTD, VTEC, Receiver Coordinates and Clock. Furthermore, one can also visualize the tracked satellites for each of the stations as well as the behavior of the filter and the observations treatment.

A new upgrade was included on the context of this work integrating an external call to

GIPSY/OASIS-II software (see section 2.3.1.) with TOMION to offer the possibility of comparing estimated parameters with a reliable external source where the set up of the processing will be done in coherence (by default) with TOMION.

A new segment has been recently added to the software to check the filter residuals and detect outliers in the input observations. Once assessed and discarded, the software will automatically re-run the *prefits* and filter segments.

In the following sections it will be summarized some of the basics of GNSS observables and its processing for the sake of understanding the software computations. However, for more detail please visit: Kleusberg and Teunissen [1996], Bernhard Hofmann-Wellenhof and Wasle [2008] and Sanz et al. [2013]. Since it applies classical equations of positioning and processing, the background for this work was taken mainly from these books.

2.2.3. Observables

In concept, the satellite navigation observables are ranges which are deduced from measured time or phase differences based on a comparison between received signals by the receiver and the ones generated by it. Unlike the terrestrial electronic distance measurements, satellite navigation uses the "one-way concept" where two clocks are involved, namely one in the satellite and the other in the receiver. Therefore, the ranges are biased by satellite and receiver clock errors and, consequently, they are denoted as pseudoranges. Thus, observables for satellite-based positioning are pseudoranges as derived from run-time observations of the coded satellite signal or from measurements of the phase of the carrier. Hence, the quantity obtained is:

$$R = c(t_r(rec) - t^s(sat)), \quad (2.1)$$

where c is the speed of light in a vacuum and $t^s(sat) = t^s + \delta^s$ is denoting the signal emission time referred to the reading of the satellite clock, and by $t_r(rec) = t_r + \delta_r$, the signal reception time referred to the reading of the receiver clock. The terms δ_r and δ^s are the errors (or biases) of the clocks with respect to a common time system (i.e. GPS time) and t_r and t^s refer to the common system time. Then, we have:

$$R = c\Delta t + c\Delta\delta = \rho + c\Delta\delta. \quad (2.2)$$

A measurement that will be called **Code**, where the terms $\rho = c\Delta t$ and $\Delta t = t_r - t^s$, $\Delta\delta = \delta_r - \delta^s$ have been introduced. The range ρ is calculated from the *true* signal travel time.

Another observable from the signal is the integrated Doppler, known as **Carrier Phase**:

$$\varphi = \rho + c\Delta\delta + \lambda N + b_r + b_s \quad (2.3)$$

where λ is the wavelength of the signal and N is a number of integer cycles, and b_r and b_s being the non-integer part of the Carrier phase ambiguity¹, among other terms not explicitly indicated here.

2.2.4. Modeling the observables

The pseudorange R measurement obtained by the receiver using this procedure includes, besides the geometric range between the receiver and the satellite and clock synchronisation

¹Note that b is not necessarily the fractional part of the total bias.

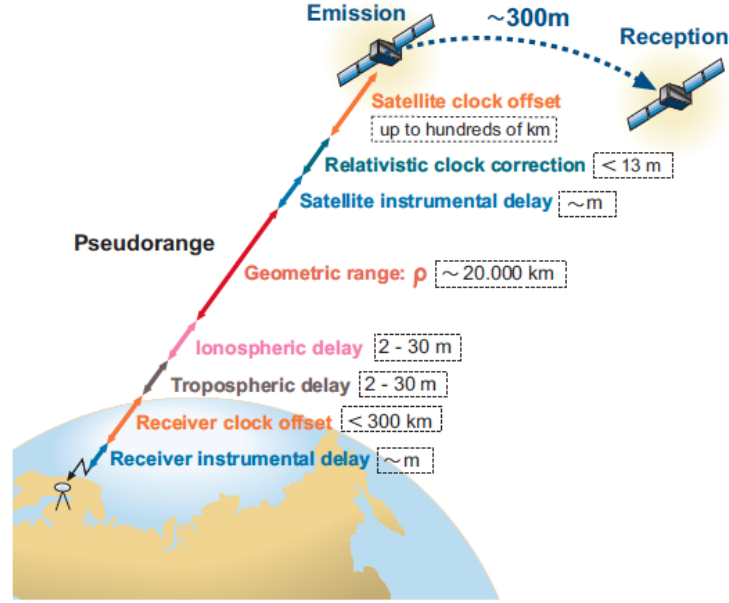


Figure 2.3: Pseudorange measurement contents. Adapted from: [Sanz et al., 2013]

errors, other terms due to signal propagation through the atmosphere (ionosphere and troposphere), relativistic effects, instrumental delays (of satellite and receiver), multipath and receiver noise (see fig. 2.4). Taking explicitly into account all these terms, the previous equation can be rewritten as follows, where R represents any GNSS code measurement at frequency f (from GPS, Glonass, Galileo or Beidou):

$$R_f = \rho + c(t_r(rec) - t^s(sat)) + T_{rec}^{sat} + I_{rec}^{sat} + K_{rec} + K^{sat} + M_{rec}^{sat} + \epsilon_{rec}^{sat} \quad (2.4)$$

Here:

- ρ is the geometric range between the satellite and receiver Antenna Phase Centres (APCs) at emission and reception time, respectively (section 5.1).
- T_{rec}^{sat} is the tropospheric delay, which is non-dispersive;
- I_{rec}^{sat} frequency-dependent ionospheric delay term;
- K_{rec} and K^{sat} are the receiver and satellite instrumental delays, which are dependent on the code and frequency;
- M_{rec}^{sat} represents the effect of multipath, also depending on the code type and frequency; and
- ϵ_{rec}^{sat} is the receiver noise.

Besides the code, the carrier itself is also used to obtain a measure of the apparent distance between satellite and receiver. These carrier phase measurements are much more precise than the code measurements (typically two orders of magnitude more precise), but they are ambiguous by an unknown integer number of wavelengths (N). Indeed, this ambiguity changes arbitrarily every time the receiver loses the lock on the signal, producing jumps or range discontinuities.

The carrier phase measurements can be modeled as

$$\Phi_f = \rho + c(t_r(rec) - t^s(sat)) + T_{rec}^{sat} - I_{rec}^{sat} + k_{rec} + k^{sat} + \lambda N_{rec}^{sat} + \lambda w_{rec}^{sat} + m_{rec}^{sat} + \epsilon_{rec}^{sat} \quad (2.5)$$

where this equation, besides the terms in equation 2.4, it includes the windup due to the circular polarisation of the electromagnetic signal and the integer ambiguity N . Note that the ionospheric term has opposite signs for code and phase. This means that the ionosphere produces an advance in the carrier phase measurement equal to the delay on the code measurement.

Generally speaking, the accuracy of code ranges is at the meter level, whereas the accuracy of carrier phases is in the millimeter range. The accuracy of code ranges can be improved, however, by the specific receiver technology or by smoothing techniques.

The disadvantage of phase ranges is the fact that they are ambiguous by an integer number of full wavelengths, whereas the code ranges are virtually unambiguous. The determination of the phase ambiguities is often a critical issue in high-accuracy satellite-based positioning.

2.2.5. Prefit

As explained in the previous section, the code and carrier phase measurements contain several additional time delays associated with the signal propagation or with the clocks, among the geometric range between the satellite and receiver antenna phase centers. These delays are common in code and carrier measurements, except among other terms, for the wind-up and the ambiguities that affect only the carrier measurements, and for a sign in the ionospheric refraction, delaying the code and advancing the carrier measurements. Figure 2.4 shows the layout of the different time delay terms in the pseudorange to illustrate the contents of the measurements. Recalling equations (2.4), the measurements can be modeled by:

$$\begin{aligned} R_f &= \rho + c(t_r(rec) - t^s(sat)) + T_{rec}^{sat} + I_{rec}^{sat} + K_{rec} + K^{sat} \\ \Phi_f &= \rho + c(t_r(rec) - t^s(sat)) + T_{rec}^{sat} - I_{rec}^{sat} + k_{rec} + k^{sat} + \lambda N_{rec}^{sat} + \lambda w_{rec}^{sat} \end{aligned} \quad (2.6)$$

where the satellite clock offset t^{sat} includes the relativistic clock correction and ρ the relativistic path correction. Note that we have excluded the multipath and error terms, since they are not easily reproduced, except for permanent geodetic receivers.

The residuals between the measured and predicted code or carrier pseudoranges contain the receiver position error and clock offset, together with mismodeling and measurement noise errors. These residuals, hereafter called prefit residuals, are the input data for the navigation equations studied in the next section. Such equations consist of a linear system whose solution by least squares or Kalman filtering allows us to decorrelate (i.e. separate) the different error components from the *prefit* residuals and then to determine the receiver coordinates and clock, or the parameters of interest, i.e. the Zenith Tropospheric Delay. The more accurate the measurement modeling, the better the decorrelation of errors and the more accurate the coordinates obtained.

Hence the term to be modeled are:

- Geometric Range (Satellite Coordinates, Relativistic Path Range)
- Correction Clock (Relativistic Clock Correction)
- Instrumental Delays (Code Measurements and Receiver Types)

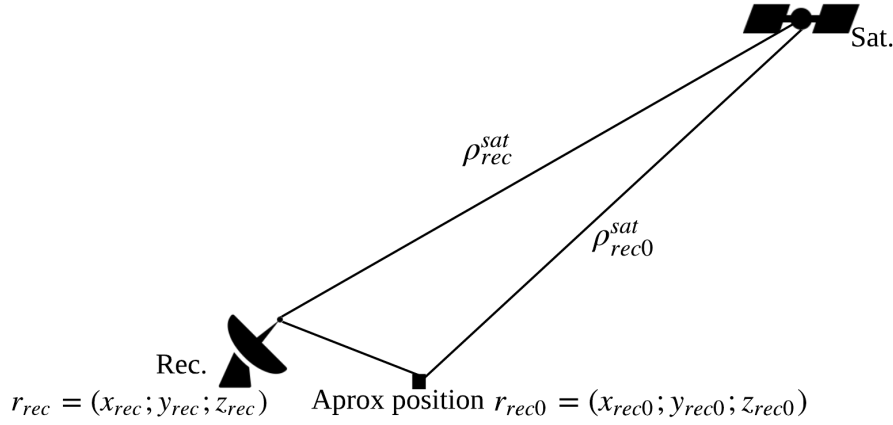


Figure 2.4: Linearization of the distance between satellite and receiver.

- Atmospheric Effects (Ionospheric Delay, Tropospheric Delay)
- Carrier Phase Wind-up Effect
- Antenna Phase Centre Correction (Antenna Phase Centre, Receiver Antenna Phase Centre, Satellite Antenna Phase Centre)
- Earth Deformation Effects (Solid Tides, Ocean Loading, Pole Tide)

We can write now:

$$Y = OBS - Model, \quad (2.7)$$

where *Model* contains all the parameters listed above in the measurement form given by the strategy and consequently with *OBS*, (see 2.2.7.).

Due to the geometric term involved in ρ , the equation to solve as to obtain the desired parameters results to be non-linear. The step that follows consists of linearizing the geometric range ρ in the neighborhood of a point $r_{rec0} = (x_{rec0}; y_{rec0}; z_{rec0})$ corresponding to the approximate position of a receiver, as shown in figure 2.4.

The the geometric range between the observing receiver site *rec* and the satellite *sat* is:

$$\rho_{rec}^{sat} = \|\mathbf{r}^{sat} - \mathbf{r}_{rec}\| = \sqrt{(x^{sat} - x_{rec})^2 + (y^{sat} - y_{rec})^2 + (z^{sat} - z_{rec})^2} \quad (2.8)$$

Then linearizing the satellite-receiver geometric range gives, for the approximate solution:

$$\rho_{rec}^{sat} = \rho_{rec0}^{sat} + \frac{x^{sat} - x_{rec0}}{\rho_{rec0}^{sat}} \Delta x_r + \frac{y^{sat} - y_{rec0}}{\rho_{rec0}^{sat}} \Delta y_r + \frac{z^{sat} - z_{rec0}}{\rho_{rec0}^{sat}} \Delta z_r, \quad (2.9)$$

where:

$$\rho_{rec0}^{sat} = \sqrt{(x^{sat} - x_{rec0})^2 + (y^{sat} - y_{rec0})^2 + (z^{sat} - z_{rec0})^2}, \quad (2.10)$$

and

$$\begin{aligned}
x_{rec} &= x_{rec0} - \Delta x_{rec}; \\
y_{rec} &= y_{rec0} - \Delta y_{rec}; \\
z_{rec} &= z_{rec0} - \Delta z_{rec}.
\end{aligned} \tag{2.11}$$

The unknowns now are the corrections to the a priori coordinates. For here on, the corrections to the coordinates will be called the unknowns.

Finally we can express:

$$Y = G \times X + \varepsilon, \tag{2.12}$$

where:

- Prefit-residuals: Y is a $(n \times 1)$ vector containing the residuals between the measured and predicted pseudoranges, "before fitting" the parameters to the linear model; including the ρ_{rec0}^{sat} ;
- Geometry matrix: G is a $(n \times m)$ matrix containing the receiver-satellite geometry. The first three elements of each row ($j = 1, \dots, n$) are the components of the unitary line-of-sight-vector;
- Unknown parameters: X is a $(m \times 1)$ vector containing the deviation between the approximated and the true coordinates ($\Delta \bullet$) and the receiver clock offset, among other terms that we will see later on; and
- Errors: ε is a $(n \times 1)$ vector containing the measurement noise and mismodeling.

Now we have a linear system of equations that involve observations with measurement errors, it is natural to assess this scene with the Least Squares Solution.

2.2.6. Filter

Due to the error term ε , in general equation 2.9 defines an incompatible system (i.e. there is no 'exact' solution fulfilling the system). In this context, the parameters' solution can be taken as the vector \hat{x} that minimizes the discrepancy in the equation system. That is, the vector provides the best fit of $y \simeq G\hat{x}$ in a given sense. Hence: to minimize the error in the least square (LS) sense we have that the solution is:

$$\hat{X} = (G^T G)^{-1} G^T Y, \tag{2.13}$$

or,

$$\hat{X} = (G^T W G)^{-1} G^T W Y, \tag{2.14}$$

where:

$$W = P^{-1} = \begin{pmatrix} 1/\sigma_{y_1}^2 & \cdots & 0 \\ \vdots & \ddots & \vdots \\ 0 & \cdots & 1/\sigma_{y_n}^2 \end{pmatrix}, \tag{2.15}$$

with n being the number of observations.

Equation 2.14 is called *The Weighted Least Square Solution (WLS)* where the measurement quality is incorporated into the fitting criterion by introducing a symmetric, positive-definite weighting matrix W . In this particular case (equation 2.15), W is taken as inverse of the covariance matrix, since σ_y is the variance of the parameter y . This is called the minimum variance criterion, where a simplification commonly used is to assume that the measurements (prefit residuals $y = (y_1, \dots, y_n)^T$) from the different satellites are uncorrelated.

2.2.6.1. Kalman Filter

The principle of Kalman filter can be roughly summarized as the *WLS* solution of the linearized observation system augmented with a prediction of the estimate as additional equations. Let $\hat{X}(k-1)$ be the estimate for the $k-1$ epoch, then a predicted estimate and the weighted solution are given as follows:

$$\begin{cases} \hat{X}^-(k) = \Phi(k-1)\hat{X}(k-1) \\ P_{\hat{X}^-}(k) = \Phi(k-1)P_{\hat{X}^-}(k-1)\Phi^T(k-1) + Q(k-1) \end{cases} \quad (2.16)$$

where:

- $\hat{X}(k-1)$ is the estimate for the $k-1$ epoch,
- $\Phi(k-1)$ is the so called the transition matrix, related to the design of the problem, and
- $\hat{X}^-(k)$ is then a prediction for the next epoch.
- $P_{\hat{X}^-}(k)$ gives the model for the covariance matrix (eq. 2.15), where
- Q is the process noise matrix.

The linearized problem will be equated as:

$$\begin{pmatrix} Y(k) \\ \hat{X}^-(k) \end{pmatrix} = \begin{pmatrix} G(k) \\ I \end{pmatrix} \times \hat{X}(k). \quad (2.17)$$

Hence the solution will be, for the *WLS* sense, the following:

$$\hat{X} = (G^T W G + P_{\hat{X}_k}^{-1})^{-1} (G^T W Y + P_{\hat{X}_k}^{-1} \hat{X}_k) \quad (2.18)$$

The algorithm can be summarized in the scheme shown in Fig. 2.5. It illustrates the three steps of the recursive filter strategy implemented in TOMION. With one first value for \hat{X}_0 , P_0 and Y_0 for initialization, one can compute \hat{X}_1 and P_1 and set this as the previous epoch estimation to reset the filter again. After a number of iterations, one will obtain the desired solution \hat{X} and P , setting up a threshold for the desired maximum difference between the final estimation and the previous one.

About the transition matrix Φ and the process noise matrix Q :

For static positioning (see sec 2.2.7.1.) it is usual to introduce:

$$Q(k) = \begin{pmatrix} 0 & 0 & 0 & 0 \\ 0 & 0 & 0 & 0 \\ 0 & 0 & 0 & 0 \\ 0 & 0 & 0 & \sigma_{\delta t}^2 \end{pmatrix} \quad \text{and} \quad \Phi(k) = \begin{pmatrix} 1 & 0 & 0 & 0 \\ 0 & 1 & 0 & 0 \\ 0 & 0 & 1 & 0 \\ 0 & 0 & 0 & 0 \end{pmatrix} \quad (2.19)$$

which in other words means that we believe the position for the previous epoch, reason why we put *ones* in the first 3 positions of the diagonal of Φ , but not for the clock (zero in the diagonal of Φ), that is highly unpredictable, so we set for it a variance $\sigma_{\delta t}^2$, in Q .

Likewise, for kinematic positioning (see sec 2.2.7.1.), we have:

$$Q(k) = \begin{pmatrix} \sigma_{dx}^2 & 0 & 0 & 0 \\ 0 & \sigma_{dy}^2 & 0 & 0 \\ 0 & 0 & \sigma_{dz}^2 & 0 \\ 0 & 0 & 0 & \sigma_{\delta t}^2 \end{pmatrix} \quad \text{and} \quad \Phi(k) = \begin{pmatrix} 0 & 0 & 0 & 0 \\ 0 & 0 & 0 & 0 \\ 0 & 0 & 0 & 0 \\ 0 & 0 & 0 & 0 \end{pmatrix}, \quad (2.20)$$

which in other words means that we forget about the previous epoch's coordinates (and clock), so set Φ to zero but we constrain (determine) the noise we would allow the process to have for each of the parameters.

There is a hybrid option which it is called *random walk*, that would allow the parameter to diverge from the previous epoch proportional (with the the derivative Q') to the time between the previous epoch and the present:

$$Q(k) = \begin{pmatrix} Q'_{dx}\Delta_t & 0 & 0 & 0 \\ 0 & Q'_{dy}\Delta_t & 0 & 0 \\ 0 & 0 & Q'_{dz}\Delta_t & 0 \\ 0 & 0 & 0 & \sigma_{\delta t}^2 \end{pmatrix} \quad \text{and} \quad \Phi(k) = \begin{pmatrix} 1 & 0 & 0 & 0 \\ 0 & 1 & 0 & 0 \\ 0 & 0 & 1 & 0 \\ 0 & 0 & 0 & 0 \end{pmatrix}. \quad (2.21)$$

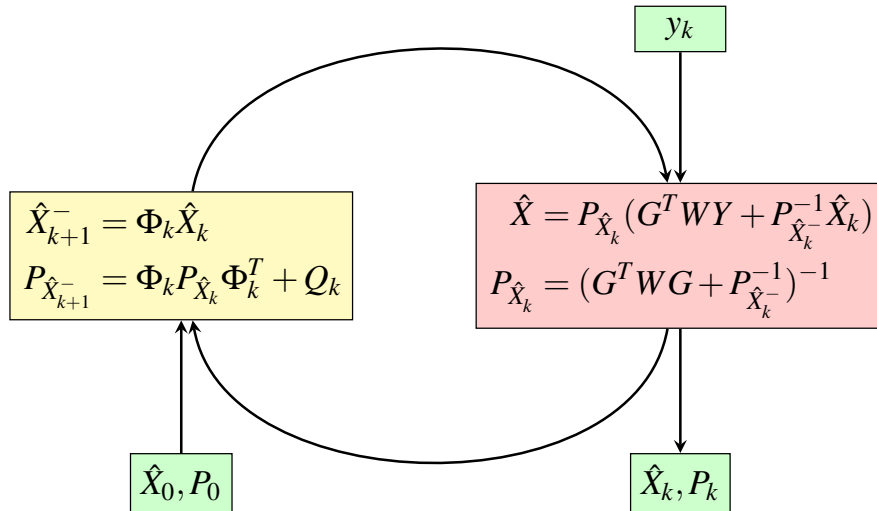


Figure 2.5: Principle of Kalman filtering.

2.2.7. Processing strategy

As it can be seen in equation 2.18 and was detailed in section 2.2.6., the prefit in Y will vary accordingly with the chosen strategy as well as the design matrix G . In this section we will focus on what are the different strategies available in TOMION for determine the unknowns in X . Also, we will focus on the strategies implemented here in this work.

TOMION offers the possibility to process the observations in different modes: Point or relative Positioning. Let us remember now what each one of them involves and the fact that TOMION was built to process in real time should be kept in mind to better understanding of its processing flux (see Fig. 2.2).

2.2.7.1. Introduction

First let us declare what *static* and *kinematic* positioning means:

- Static: receiver whose coordinates are to be defined is not moving.
- Kinematic: receiver whose coordinates are to be defined is moving.

Static denotes a stationary observation location, while kinematic implies motion. A temporary loss of signal lock in static mode is not as critical as in kinematic mode.

Real-time processing versus post-processing: For real-time GNSS, the results must be available in the field immediately. The results are denoted as “instantaneous” if the observables of a single epoch are used for the position computation and the processing time is negligible. The concept of modern operational satellite techniques aims at instantaneous navigation of moving vehicles (i.e., cars, ships, aircraft) by unsmoothed code pseudoranges. A different and less stringent definition is “quasi (or near) real-time” which includes computing results with a slight delay. Today, radio data links allow the combination of measurements from different sites in (near) real time. Post-processing refers to applications when data are processed after the fact. The loss of data is no longer an issue and the modeling can be done carefully.

On the other hand, here we present the work done in *real time-like* mode. It implies that all the corrections will be accounted for as if they were processed in real time, that is, only broadcasted ephemeris and satellite clock will be used for Precise Point Positioning (PPP) and forward filter for relative positioning. The advantage of not performing the computations in real time is only anecdotal and for the sake of simplicity of the data handling.

2.2.7.2. Absolute Positioning

The coordinates of a single point are determined by point positioning when using a single receiver which measures pseudoranges to four or more satellites. The terms “point positioning”, “single-point positioning”, and the term “absolute point positioning” are synonymously used. The term “absolute” reflects the opposite of “relative”.

Now we need to account for the satellite clock error in Eq. 2.6, because if we take it as an unknown we would add one unknown for each additional satellite observed since it adds one equation with the same site coordinates but with a new satellite clock bias. Thus, there would always be more unknowns than measurements. Even when an additional epoch is considered,

new satellite clock biases must be modeled due to clock drift. Fortunately, the satellite clock information is known with sufficient accuracy for absolute positioning (and it cancel out in relative mode) and transmitted via the broadcast navigation message, e.g., in the form of three polynomial coefficients a_0 , a_1 and a_2 , and specially the usage of precise real-time transmitter clocks like the ones provided by IGS. Without them being accounted for, the pseudoranges would contain hundreds of kilometers of error and this situation would yield unacceptable results. It should be noted that the polynomial removes a great deal of the satellite clock uncertainty, but a small amount of (random) error remains. Furthermore, for an improved correction one should include the relativistic term.

Nevertheless, some considerations must be taken into account. If the number of observations is n_s , n_t , where n_s denotes the number of satellites and n_t the number of epochs, for static point positioning with the code, the three coordinates of the observing site and the receiver clock bias for each observation epoch are unknown. Thus, the number of unknowns is $3 + n_t$. The basic configuration is defined by:

$$n_t n_s = 3 + n_t, \quad (2.22)$$

The receiver coordinates in the geometric term given by 2.9 and the the receiver clock offset are the 4 main unknowns for this problem. Therefore, we have 4 unknowns for each pair satellite-receiver and epoch of time observed. Since for kinematic positioning $n_t = 1$, thence at least 4 satellites must be tracked simultaneously.

For static point positioning with phase, the number of unknowns is composed of 3 coordinates of the observing station, one unknown ambiguity per satellite and one clock error unknown receiver. Hence, the minimum number of observations to get a solution is 5. Note that, solutions for a single epoch do not exist for point positioning with carrier phases. As a consequence, kinematic point positioning with phases is only possible if the phase ambiguities are known from some initialization, or the user can wait the best part of one hour. In this case, the phase range model converts to the code range model.

Considering the positioning being done simply from R or φ , the main limiting factors with respect to the achievable accuracy are the orbit errors, the clock errors, and the atmospheric influences (ionospheric and tropospheric refraction), therefore the results obtained from this procedure would not be better than a few meters, although it would theoretically suffice.

PPP Strategy:

The Precise Point Positioning technique allows centimeter-level accuracy to be achieved for static positioning and decimeter level, or better, for kinematic positioning, where the coordinates are treated as white-noise parameters in the navigation filter. This high accuracy requires accurate measurement modeling, where all model terms described in the section 2.2.5. must be taken into account (up to centimeter level or better). Precise point positioning uses accurate orbital data and accurate satellite clock data (as provided, e.g., by the IGS), and dual-frequency code pseudoranges and/or carrier phase observations by definition, Zumberge et al. [1997]. The preferred model is based on an ionosphere-free combination of code pseudoranges and carrier phases as well:

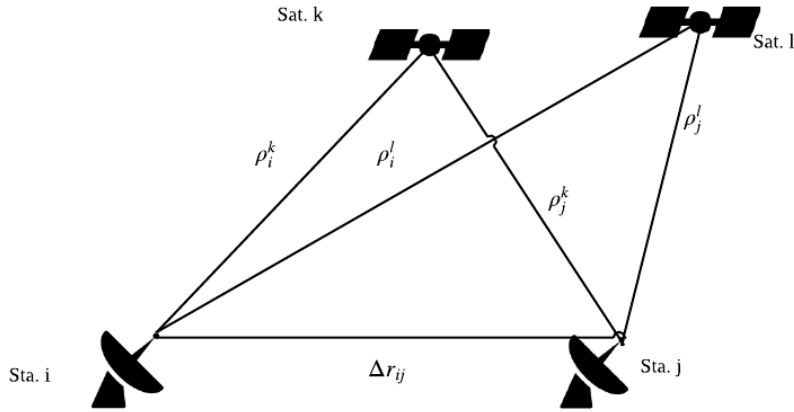


Figure 2.6: Basic concept of relative positioning.

$$\begin{aligned}
 R_c &= \frac{f_1^2 R_1 - f_2^2 R_2}{f_1^2 - f_2^2} \\
 \Phi_c &= \frac{f_1^2 \Phi_1 - f_2^2 \Phi_2}{f_1^2 - f_2^2}
 \end{aligned} \tag{2.23}$$

Equating A.4 with 2.4 and 2.5 we have:

$$\begin{aligned}
 \frac{f_1^2 R_1 - f_2^2 R_2}{f_1^2 - f_2^2} &= \rho + c(t_r(rec) - t^s(sat)) + \Delta T_{rec}^{sat} \\
 \frac{f_1^2 \Phi_1 - f_2^2 \Phi_2}{f_1^2 - f_2^2} &= \rho + c(t_r(rec) - t^s(sat)) + \Delta T_{rec}^{sat} + \frac{f_1^2 N_1 - f_2^2 N_2}{f_1^2 - f_2^2}
 \end{aligned} \tag{2.24}$$

The unknown parameters to be determined are: the receiver position contained in ρ , which also would be linearized, the receiver clock error, the tropospheric delay ΔT_{rec}^{sat} , and the ambiguities N_1 and N_2 . Based on this model, PPP may be applied either in static or in kinematic mode.

The right hand side of equation 2.24 is a linear combination of two observables, hence, since the frequencies are known parameters, these quantities can be computed. On the other hand, the modeling can be performed identical to 2.6 and converted with the mentioned parameters, the frequencies. Finally, the prefit will be calculated by subtracting the model to the observation.

Note that strictly speaking, the tropospheric delay ΔT_{rec}^{sat} , is not necessarily to be determined by the filter. One could also determine the total delay and move it to the prefit term or, as it was done in this work, to carefully determine an a priori model (see sec. 2.2.9.) and estimate with the filter the residual part as a parameter (random walk process).

2.2.7.3. Relative Positioning

Instead of “relative positioning” the term “differential positioning” is often used. Note, however, that the two methods are (at least theoretically) different. Differential positioning is rather an improved single-point positioning technique and is based on applying (predicted) corrections to

pseudoranges measured at an unknown site. The technique provides instantaneous solutions (usually denoted as real-time solutions) where improved accuracies with respect to a reference station are achieved.

Relative positioning is possible if (as in the case of differential positioning) two receivers are used and (code or carrier phase) measurements, to the same satellites, are simultaneously made at two sites. The measurements taken at both sites are (in contrast to differential positioning) directly combined. This direct combination further improves the position accuracy but prevents instantaneous solutions in the strict sense. Normally, the coordinates of one site are known and the position of the other site is to be determined relatively to the known site (i.e., the vector between the two sites is determined). In general, the receiver at the known site is stationary while observing.

The objective of relative positioning is to determine the coordinates of an unknown point with respect to a known point which, for most applications, is stationary. In other words, relative positioning aims at the determination of the vector between the two points, which is often called the baseline vector or simply baseline (Fig. 2.6).

Single differences: Two receivers and one satellite are involved. We mitigate the clock error of the satellite (we assume that we have eliminated it).

$$\begin{aligned}\Delta R_{ij}^k &= \rho_i^k - \rho_j^k + c(\delta_i - \delta_j) + I_i^k - I_j^k + T_i^k - T_j^k \\ \Delta \phi_{ij}^k &= \rho_i^k - \rho_j^k + c(\delta_i - \delta_j) - I_i^k + I_j^k + T_i^k - T_j^k + N_i^k - N_j^k\end{aligned}\quad (2.25)$$

Double differences: Two receivers and two satellites are involved. We mitigate the clock error of the satellite and the receiver (we assume that we have eliminated them).

$$\begin{aligned}\Delta \nabla R_{ij}^{kl} &= \rho_i^k - \rho_j^k - (\rho_i^l - \rho_j^l) + I_i^k - I_j^k - (I_i^l - I_j^l) + T_i^k - T_j^k - (T_i^l - T_j^l), \\ \Delta \nabla \phi_{ij}^{kl} &= \rho_i^k - \rho_j^k - (\rho_i^l - \rho_j^l) - I_i^k + I_j^k - ((-I_i^l + I_j^l)) + T_i^k - T_j^k - (T_i^l - T_j^l) + N_i^k - N_j^k.\end{aligned}\quad (2.26)$$

Or in a more compact form we can write:

$$\begin{aligned}\Delta \nabla R_{ij}^{kl} &= \Delta \nabla \rho_{ij}^{kl} + \Delta \nabla I_{ij}^{kl} + \Delta \nabla T_{ij}^{kl}, \\ \Delta \nabla \phi_{ij}^{kl} &= \Delta \nabla \rho_{ij}^{kl} - \Delta \nabla I_{ij}^{kl} + \Delta \nabla T_{ij}^{kl} + \Delta \nabla N_{ij}^{kl}.\end{aligned}\quad (2.27)$$

where:

$$\Delta \nabla \bullet_{ij}^{kl} = \bullet_i^k - \bullet_j^k - (\bullet_i^l - \bullet_j^l) \quad (2.28)$$

Static: The static relative positioning method is most commonly used for geodetic surveys. The required observation periods depend on the baseline length, the number of visible satellites, the number of carrier frequencies, and the geometric configuration. The accuracy is correlated with the baseline length and amounts to 1 to 0.1 ppm for baselines up to some 100 km and even better for longer baselines.

Static relative positioning also includes the rapid static technique based on fast ambiguity resolution techniques. These techniques generally use code and carrier phase combinations on all frequencies. Restricting the method to 20 km baselines, accuracies at the subcentimeter level can be achieved.

Typical applications of static surveying include state, county, and local control surveys, photo-control surveys, boundary surveys, and deformation surveys.

Kinematic : Kinematic surveys are the most productive in that the greatest number of points can be determined in the least time. The drawback is that after initialization of the survey a continuous lock on at least four satellites must be maintained.

The kinematic technique requires the resolution of the phase ambiguities before starting the survey. The initialization can be performed by static or kinematic techniques. Although the on-the-fly techniques allow to initialize while the receiver is in motion, the initial integer resolution can be accomplished more rapidly with the receiver being static. Dual-frequency receivers require up to 1 or 2 minutes of observations for baselines up to 20 km to resolve the ambiguities kinematically.

After initialization no loss of lock should occur, otherwise initialization has to be restarted. Triple-frequency receivers will allow to resolve the ambiguities instantaneously, i.e., epoch by epoch. Solutions of several epochs, however, are needed to mitigate the risk of false ambiguity fix.

RTK: The objective of relative positioning is to reduce or even eliminate error sources by differencing GNSS measurements taken at different stations at the same epoch. Best accuracies are achieved in the relative positioning mode with observed carrier phases. Originally, relative positioning was conceived for post-processing. Thus, this method was and still is particularly used for surveying and geosciences. Today, real-time data transfer is routinely applied, which enables realtime computation of baseline vectors up to few tens of km and has led to the real-time kinematic (RTK) technique.

WARTK : Transmitting the phase measurement in real time from the base station to the rover, the ambiguities can be also solved in real time, leading to the RTK method. The decorrelation of the error sources limits the relative methods to about 20 km. The wide-area RTK (WARTK) method avoids a fast decorrelation of the error sources by implementing ionospheric corrections. In this way the ionospheric influence is significantly reduced or even eliminated and the integer nature of the ambiguities is preserved. The later characteristic allows to fix wide-lane ambiguities and to achieve subcentimeter accuracies despite the baseline lengths of up to 400 km. Similar to RTK, also WARTK takes several minutes before the solution converges using dual-frequency receivers. Triple-frequency receivers allow to instantaneously solve the ambiguities for a baseline length of about 20 km in traditional RTK mode and up to 400 km in WARTK operation [Hernández-Pajares et al., 2004].

As it can be seen on table 2.2, some aspects of relative positioning are unmatched by any other strategy that could be implemented in real time. Its advantage of cancelling (or at least practically cancel) the satellite clock error, brings much simplicity to the method. However, unless it is approached in the WARTK sense, where closeness to a reference station is not as critical, the relative positioning is not always the most suited one. The independence of a close site together with the required bandwidth and the error propagation due to the combination of four measurement has made the Point Precise Positioning become more and more interesting this last decade. Its main drawback is the constant update of the satellite clock offset correction and orbits, which are only a few coefficients.

Relative Positioning	Precise Point Positioning
✓ Satellite clock error	✗ Satellite clock error
✗ Close to a Station	✓ Independent
✗ bandwidth	✓ bandwidth
✓ Modeling terms	✗ Modeling terms
✓ Accuracy	✗ Accuracy
✗ Error Propagation	✓ Error Propagation

Table 2.2: Relative Positioning vs. Precise Point Positioning

2.2.8. Ambiguity resolution

2.2.8.1. Introduction

The ambiguity inherent with phase measurements depends upon both the receiver and the satellite. There is no time dependency as long as tracking is maintained without interruption. As soon as the ambiguity is determined as an integer value, the ambiguity is said to be resolved or fixed. In general, ambiguity fixing strengthens the baseline solution. For the integer-fixed solution, the precision of the coordinates is below the 1 cm level. But sometimes introducing the float ambiguities (i.e., real values) solutions may be enough for certain applications.

For absolute or relative positioning, the ambiguities need to be introduced as parameters to be determined by the navigation equations. The use of double-differences for carrier phase is a very convenient approach since prevents an effective separation of the integer ambiguities from the receiver clock offset, considering the latter has been eliminated and the isolation of the ambiguities is possible.

Making use of the different combination of observables (see Appendix A.2.), TOMION introduces assorted approaches for ambiguities resolutions. For undifferentiated phase ranges we can obtain from:

- the ionosphere free combination:

$$B_c = b_c + \frac{2}{2}(\lambda_N N_N + \lambda_W N_W); \quad (2.29)$$

- the geometry free combinations:

$$B_I = b_I + \lambda_1 N_1 - \lambda_2 N_2 = B_1 - B_2 \quad (2.30)$$

- the geometry and ionosphere free combinations, the Melbourne-Wübbena combination:

$$B_{MW} = \lambda_W (N_1 - N_2) + b_W \quad (2.31)$$

where: λ_\bullet is the wavelength for the • frequency or combination; N_\bullet is *Integer ambiguity* for the • frequency or combination; B_\bullet is the *Float ambiguity* for the • frequency or combination, i.e. the total *bias*; and $b_\bullet = b_{rec} - b^{sat}$ is the *fractional ambiguity* for the • frequency or combination.

Now, in a 2 by 2 system of equation we have that our targets are the *Integer ambiguities* N_1 and N_2 . Imagine that we compute the Melbourne-Wübbena combination and the geometry free

combination, we can obtain our unknowns N_1 and N_2 and introduce them in the ionosphere free combination. As they would no longer be a parameter for the navigation equations, the convergence of the Kalman filter could be considerably faster and the results on the other estimates more precise and accurate. Likewise, the analogous procedure can be done for introducing the *Integer ambiguities* N_1 and N_2 in the geometry free combinations and make use of the filter estimate to study the ionosphere delay [Hernández-Pajares et al., 2000c]. This technique can be further exploited by the user for what TOMION offers versatility if handled with judgment.

2.2.8.2. Cycle Slip Detection

When a receiver is turned on, the fractional part of the beat phase (i.e., the difference between the satellite-transmitted carrier and a receiver-generated replica) is observed and an integer counter is initialized. During tracking, the counter is incremented by one cycle whenever the fractional phase changes from 2π to 0. Thus, at a given epoch, the observed accumulated phase $\Delta\phi$ is the sum of the fractional phase ϕ and the integer count N . The initial integer number N of cycles between the satellite and the receiver is unknown. This phase ambiguity N remains constant as long as no loss of the signal lock occurs. In this event, the integer counter is reinitialized, which causes a jump in the instantaneous accumulated phase by an integer number of cycles. This jump is called a cycle slip which, of course, is restricted to phase measurements.

In TOMION, the cycle slip detection is performed mainly with the Geometry Free (ϕ_I) combination. This procedure involves computing the difference of two consecutive epochs of the combination twice. This is:

$$\phi_I^2 = \phi_I(t+1) - \phi_I(t) - [\phi_I(t) - \phi_I(t-1)] = \phi_I(t+1) - 2\phi_I(t) + \phi_I(t-1) \quad (2.32)$$

where: superscripts indicate the order of the difference and the subscripts, the epoch of the observation. Note that, as it is as the second derivative any data irregularity would be amplified and, thus, the improved possibility of detecting the jump.

There is a pathological case where the jump in ϕ_1 is proportional to the jump in ϕ_2 (by a constant equal to 154/120 in the case of GPS signals) that would bring to zero the bias in ϕ_I and the procedure would not detect the anomaly. Hence, in the case L_I happens to fail, there is a second check done with MW combination.

By performing the single difference in time of the Melbourne-Wübbena combination:

$$MW^1 = B_W(t+1) - B_W(t) - [D_n(t+1) - D_n(t)] \quad (2.33)$$

This means that a change between two epochs of the MW combination corresponds such change in the *wide lane* ambiguity B_W and the corresponding for the D_n , the instrumental delay in the *Narrow Lane*. Since the instruments delay do not change for two consecutive epochs, the MW^1 is directly the change in B_W . Now, we have that $B_W = \lambda_W N_W$, and $N_W = N_1 - N_2$. If δ means single difference in time, hence:

$$\delta B_{MW} = \delta N_1 - \delta N_2 \quad (2.34)$$

Therefore, is the bias is such that the ϕ_I does not reflects it, then the jump can be seen in eq. 2.34, which is never equal to zero. Although this last combination seems to be the most

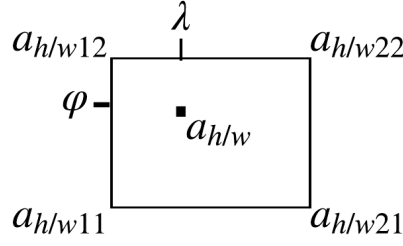


Figure 2.7: Bilinear interpolation.

suited one because it has the longer wavelength, it involves working with the code that is much noisier than the phase.

A third check is be done with the difference in time of the double differences of the prefit of the *Ionospheric Free combination* but we will not go into much detail here.

2.2.9. TOMION's Mapping Functions

As a result of this work, the software gives the user the option of computing the *a priori* ZTD with two different mapping functions: not only Niell Mapping Functions (NMF) but also Vienna Mapping Functions (VMF). One of the main focuses of this work was to upgrade the present mapping function implemented on TOMION, i.e. NMF [Niell, 1996], to a more modern one. This function has been successfully accounting for the the projection of the slant tropospheric to the zenith delay for over 20 years on TOMION in WARTK mode (see Hernández-Pajares et al. [2000b]). For this classical Niell implementation, the Zenith Hydrostatic Delay is computed with Saastamoinen and the Zenith Wet Delay *a priori* is constant and equal to 10 cm. The addition of this two quantities multiplied by its respective NMF (i.e. the hydrostatic and wet), constitute the Zenith Tropospheric Delay (ZTD) *a priori* for the filter, for the first option.

The development of an improved empirical model for tropospheric slant delays presented in [Böhm et al., 2015] is thought to provide the user with the slant delay and would come to make the trade off between computational expense and complexity. For geodetic processing as it is aimed here, this approach could be used as an *a priori* value for the *prefit* model.

For the new mapping function, we have taken the subroutine from *GPT2w* (see section 1.2.3.3.), called *gpt2_1w*, to compute the meteorological parameters needed as inputs for the computations of the zenith delays wet and dry. This subroutine determines pressure, temperature, temperature lapse rate, mean temperature of the water vapor, water vapor pressure, hydrostatic and wet mapping function coefficients a_h and a_w , water vapor decrease factor and geoid undulation for specific sites near the Earth surface. It is based on a 1 x 1 degree external grid file ('gpt2_1wA.grd') with mean values as well as sine and cosine amplitudes for the annual and semiannual variation of the coefficients.

As it was explained in section 1.2.3.3., the grid values were determined by numerical integration of the wet refractivity along the site vertical (Nilsson et al. 2013), allowing to simply invert Λ toward a global k grid, which will be very much representative of the decrease factor behavior through the entire troposphere and fully consistent with the zenith wet delay.

The parameters that will be used output from this subroutine are: pressure (P), mean tem-

perature of the water vapor (T_m), water vapor pressure (e_s), and water vapor decrease factor (Λ). As it can be seen in Fig. 2.8, this subroutine makes use of the station coordinates in ellipsoidal system latitude, longitude and height (ϕ , λ and h , respectively) and the modified Julian day (mjd). On one hand, the pressure is only used for the computation of the Zenith Hydrostatic Delay (ZHD) within Saastamoinen function (see eq. 1.4). On the other hand, the mean temperature of the water vapor, water vapor pressure, and water vapor decrease factor, are used for computing the *a priori* Zenith Wet Delay (ZWD_0) in the Askne and Nordius [1987] empirical approximation (see eq. 1.7).

The coefficients b_h , b_w , c_h and c_w of the mapping functions take the form in equations 1.11, 1.12, 1.13 and 1.14, respectively, and only the latitude is needed for this. For a_h and a_w , the software downloads the files from GGOS [2017] that contain gridded values every 2° in latitude, 2.5° in longitude and every 6 hours, instead of using the ones modeled and available in the grid *gpt2.1w*. The a_h and a_w downloaded each 6 hours are slightly better than the ones provided by the grid, but this is not the only reason why we chose to do it this way. Also, it would give the software the option of not relying on the grid, when for example measurements from temperature and pressure are available. Furthermore, as it will be done in the near future, for IGS sites, retraced parameters could be introduced in this philosophy.

Hence, for the streamed files, bilinear interpolation (Fig. 2.7) with the 4 closest points, in space and linear in time is performed for the station coordinates, as it is shown below. This is the same procedure the subroutine does when it computes the parameters for the given coordinates.

For the spatial interpolation we have:

$$a_{h/w}^t = \left[a_{h/w22}^t (\lambda_2 - \lambda) + a_{h/w21}^t (\phi_2 - \phi) + a_{h/w12}^t (\lambda - \lambda_1) + a_{h/w11}^t (\phi - \phi_1) \right] \times \frac{1}{A} \quad (2.35)$$

where:

- ϕ and λ are the station latitude and longitude, respectively.
- $A = (\lambda_2 - \lambda_1) \times (\phi_2 - \phi_1)$, the beam surface;
- t is the epoch before the observation where files are available, i.e.: 00, 06, 12 and 18hs (UTC);
- subscripts h or w stand for the hydrostatic or wet mapping function;
- t_0 is the epoch of the observation; and
- $*_{11}$ is the value of the parameter $*$ on the grid point in the bottom left and so on.

And for the temporal:

$$a_{h/w}^{t_0} = a_{h/w}^t + (a_{h/w}^{t+1} - a_{h/w}^t)(t_0 - t) \quad (2.36)$$

The following details have been taken into account:

1. The first file of the following day is also downloaded and denoted as the data belonging to the hour 24 of the day of the current epoch. Hence, 5 files per day are needed.
2. For stations between the meridian 357.5° and 360° , the spatial interpolation was done with values for the Greenwich meridian.

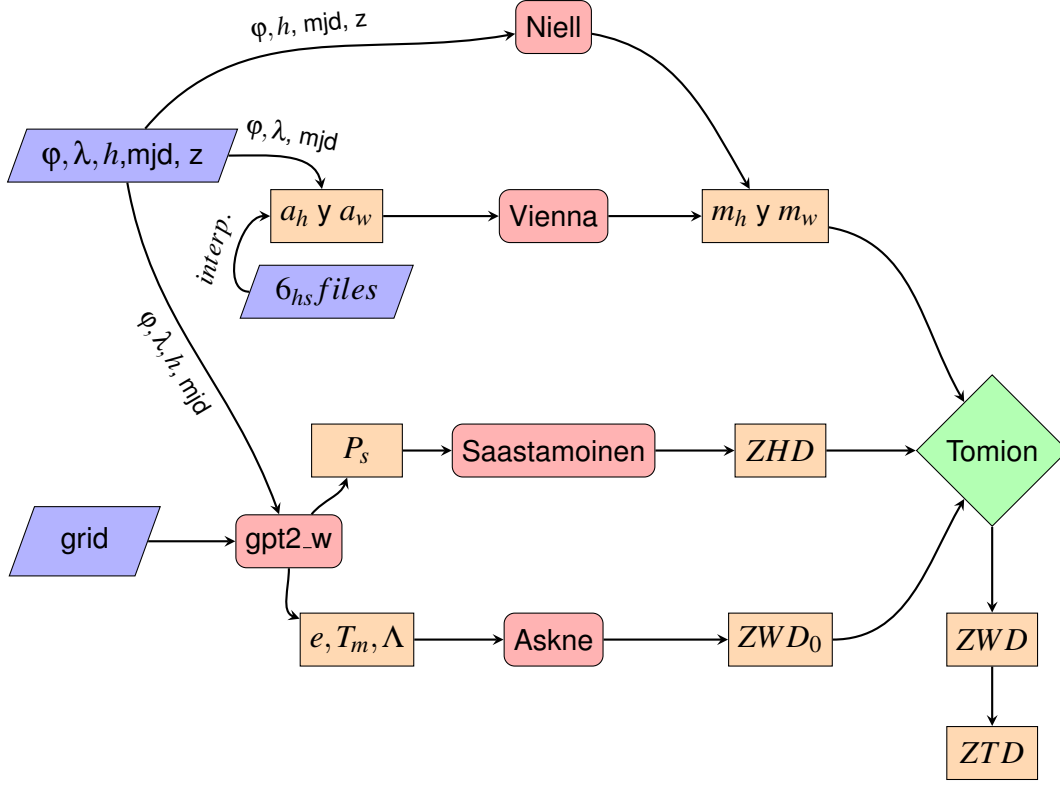


Figure 2.8: TOMION's mapping functions.

3. The resolution in φ and λ and its starting and ending points have been read from the headers of the files, so if it changes, it would be consistent.
4. The sign of the increment in φ and λ is given implicitly by the difference of 2 consecutive values.

Once the interpolation for a_h and a_w has been done and we have calculated through *gpt2.1w*, the atmospheric parameters we compute the *ZHD*, *ZWD* and *VMF wet* and *dry* and with the corresponding functions. Note that, although this subroutine gives a value for a_h and a_w , we have computed anyway the value interpolated from the files, and have compared results from both sources and the latter one seemed to be the most fitted one.

Summarizing, the computations rely on 4 previous calculations:

- *gpt2.1w* (1.2.3.3.);
- Saastamoinen (see eq. 1.4);
- Askne (see eq. 1.7);
- Interpolations; and
- VMF1 (see 1.2.3.2.);

The subroutine written for this work, involves all the steps drawn to the left of TOMION's icon in figure 2.8, and it is in charged of computing the Zenith tropospheric delay a priori for the *prefit*. Furthermore, the mapping functions are involved in the designed matrix (see *G* in sec. 2.2.5.)

2.3. External sources

In order to be able to compare the Zenith Tropospheric Delay estimates on hands of TOMION, we decided to include the International GNSS Service (IGS) final product for such error. This values are only available for IGS sites and it is not always the case for parameter estimation. As it will be shown in chapter 3, a second reference (from GIPSY) had to be included for comparing with the in-house computations.

2.3.1. GIPSY

GIPSY/OASIS-II [Zumberge et al., 1997], or GIPSY, is the GNSS-Inferred Positioning System and Orbit Analysis Simulation Software package. GIPSY is developed by the Jet Propulsion Laboratory (JPL), and maintained by the Near Earth Tracking Applications and Systems groups.

Under the IonSAT group valid license for this software, the Zenith Troposphere Delay (ZTD) was calculated for the same data set than for the in house source. Both mapping functions were implemented and compared consequently and it's commands were integrated in TOMION's computations as a separate module for the sake of comparing the internal estimates with another external source.

GIPSY/OASIS cannot, or at least not easily, use normal equations as standard algorithm, because clock and other biases are treated as stochastic variables. This applies also to the wet component of the tropospheric zenith delay, while the dry part is assumed to be constant as predicted by a model. Thus, the estimates of the wet delay include also variations of the dry component, unless one includes the call to an optional function which computes an *a priori* value for the dry component.

The *tropnominal* function allows to compute values for the an specific site, whose coordinates must be introduced in degrees (latitude and longitude) and in meters (height), and for a given interval of time (not necessarily a day), which a sampling time *and* mapping function to choose the user. Therefore, for each run, i.e. Neil or Vienna mapping function in TOMION, *tropnominal* is set in concordance with. Once the *a priori* terms were computed, its estimates were introduced to the filter as the *a priori* values for the ZTD parameters. Again, the filter module has the option for introducing a mapping function for the design and then it was also specified to the corresponding mapping function.

For the implementation of VMF1, it needs to be fed with the parameters a_h and a_w for the time interval of the study plus one day before and one day after, which are streamed from GGOS [2017], like for TOMION implementation of the mapping function. Although, the format is not the same, which increases the computational time, but the effort of making use of the same file will be done in the near future.

For procedures inherent to GIPSY, that we will not go into much detail in this manuscript, it is not efficient to process in double difference mode for large networks like the one we used for this study. Therefore, the network solutions with GIPSY/OASIS were performed in the precise point positioning mode which leads to position estimates of all stations independently of each other.

2.3.2. IGS

The International GNSS Service provides, on an openly available basis, high-quality GNSS data, products and services in support of the terrestrial reference frame, Earth observation and research; positioning, navigation and timing; and other applications that benefit science and society, such as the Zenith Troposphere Delay product, which will be used here to compare with TOMION's estimations of the given parameter.

The IGS network is a collection of a number of stations operated by many different organizations in sight of a common good. Participating stations must agree to adhere to the standards and conventions settled by this organization, for ensuring the consistent high quality of the IGS network and products. Of particular importance to the IGS is the stable, long-term operation of the network. Furthermore, some of the stations contribute to the realization of the International Terrestrial Reference Frame (ITRF).

IGS associate analysis centers generate troposphere products from ground-based GNSS data. These products include five-minute estimates of zenith path delay (ZPD) and north and east troposphere gradient components. Data are available in daily files by site for over 350 GNSS stations in the IGS network. Measurements of surface pressure and temperature at GNSS sites allow the extraction of precipitable water vapor from the total zenith path delay. Final troposphere estimates for over 350 stations in the IGS network. The troposphere products utilize the IGS final satellite, orbit, and EOP products and are therefore available approximately three weeks following the observation day. Troposphere products are available in a standard, IGS format. The format is *sinex* and with an accuracy of 4mm and a latency of 4 weeks at most. For further information visit IGS [2017].

Chapter 3

RESULTS

3.1. Introduction

The initial aim of this work was to assess the Zenith Tropospheric Delay (ZTD) estimates from TOMION, and, by extension, the accuracy of the geometric modeling part. The data that was originally going to be considered was related with a flight performed in the East of Australia. However, in order to have a reference value to compare with, it was only pursued with data from IGS sites. Nevertheless, as this was inspired by the flight and it is of our interest to be able to estimate the ZTD on the plane receiver in the near future, we continued working with stations in the area, and for the date of the flight, 22nd and 23rd of April of 2014, also because other members of the research group are engaged with ambiguity fixing and determination of the Vertical Total Electron Content (VTEC) for the same data set.

We have compared TOMION estimates against IGS products and an in built module call to external GIPSY/OASIS-II software [Zumberge et al., 1997] licensed by JPL (Jet Propulsory Laboratory) to UPC, that would be of much use when IGS-ZTD are not available to contrast with. The main focus of this work was to refine the troposphere mapping function, therefore Vienna Mapping Function (VMF) was included as a further option in addition to the Niell Mapping Function (NMF) already functional in the software and a comparison between them was carried out. Moreover, we have tried out two different processing modes: Precise point Positioning (PPP) and Relative positioning, Wide Area Real Time Kinematics (WARTK) *like*¹ mode. Finally, it was tested the performance of a new post-processing filter in the software to eliminate the observations outliers.

The totality of the results can be seen in the appendix to maintain it clear enough. However, we have not included in the main text the statistics of all of the results obtained. The best results of all the combinations was chosen to be a starting point for further results in the main analysis presented here.

3.2. First Computations

In this section we will briefly comment the most raw results that were the starting point of the current transcript. As it was described in section 2.1., the data set consists of 2 days of GPS observations over the South east of Australia gathered of 7 permanent IGS receivers, for which the IGS-ZTD final product is available to contrast with. The software was mostly running in relative mode disconnecting the ionospheric modeling and for precise dual frequency at the time.

¹see sec. 2.2.7.3.

3.2.1. Process Noise

In the very first steps of studying the ZTD computed with TOMION we obtained estimates like we show in Fig. 3.1. The curves (red) follow the reference (green) on a larger scale, however, it seems that the ZTD estimates show a latency of about 3000 to 6000 seconds (half to one hour) with respect to the reference for some of the sites, and a positive bias of about 2 cm or more in some of the cases. The observation of this two effects (or potential errors) were the main drivers of this work.

In the first place, we started out with updating the Ocean Tide Loading (OTL) files and the Antenna Phase Center (APC) Offset file for both the receiver and the satellite antennas, as recommended on Haase et al. [2003] as a possible systematic error source, together with the mapping functions, in the ZTD estimation. The results, that are not shown here, were not significantly modified by this. Moreover, the bias and latency persisted.

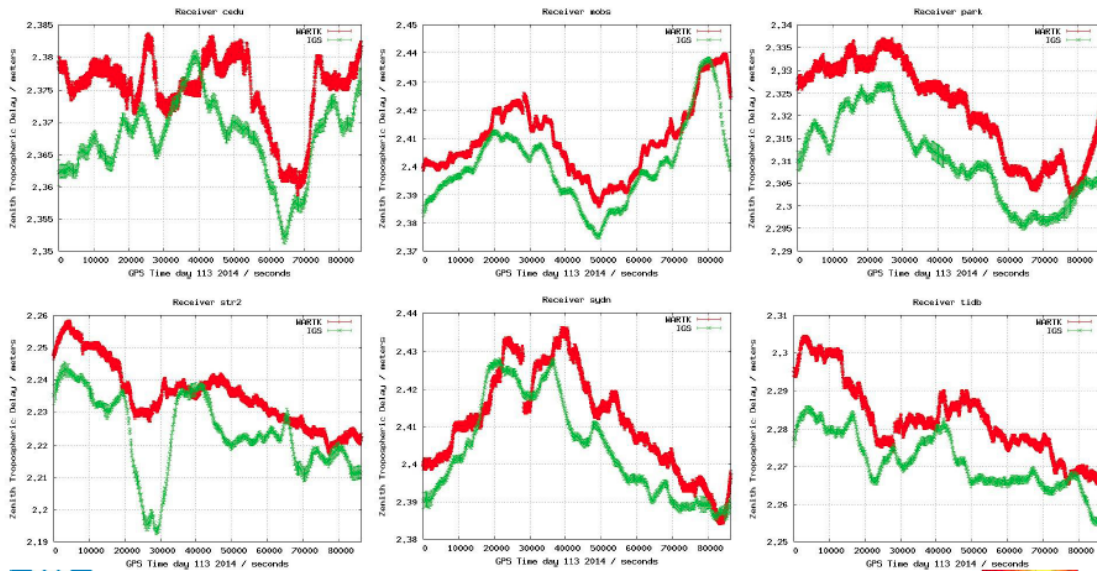


Figure 3.1: First computations of ZTD². In red TOMION estimates, in green the IGS product.

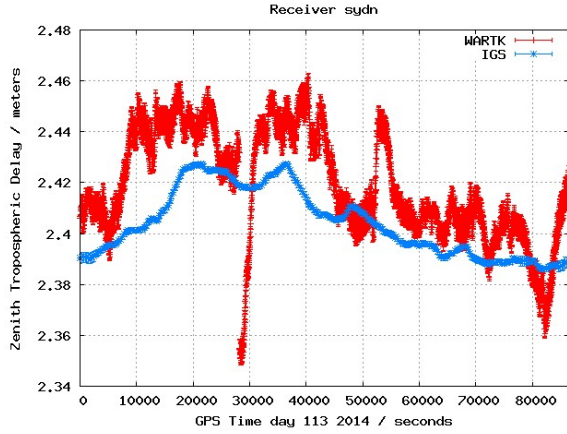
Before we moved to the update of the NMF implemented at the time to a more modern one, we decided to change the variance (σ in eq. 2.15) of the *ZTD* modeled like a random walk process, i.e. process noise in the so called *process noise matrix* Q (see sec. 2.2.6.1.) from 1mm^2 to 1cm^2 per hour. The smaller variance was producing that the estimates kept information from the previous epochs in the random walk process resulting in delaying the estimates. Low variances in the matrix can make the update of the filter with information of the present epoch too slow.

We had mended the latency with this change and hence improved our estimates of the ZTD. However, the results still were approximately 2 cm larger than the IGS products. We have not included a figure here, but the time shift with respect to the references can be seen in figures A.1 and 3.8, together with other improvements.

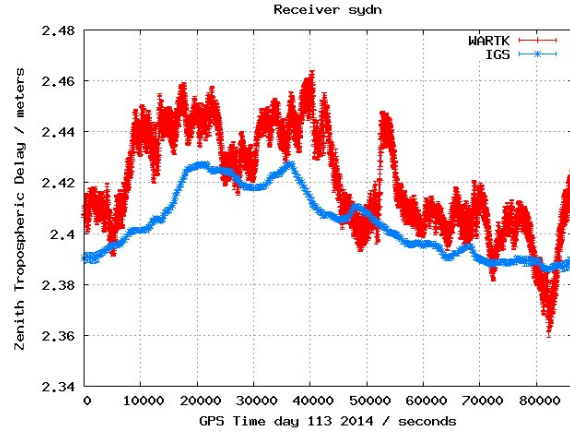
²*tid1* not shown here

3.2.2. The tropospheric delay as a quality factor

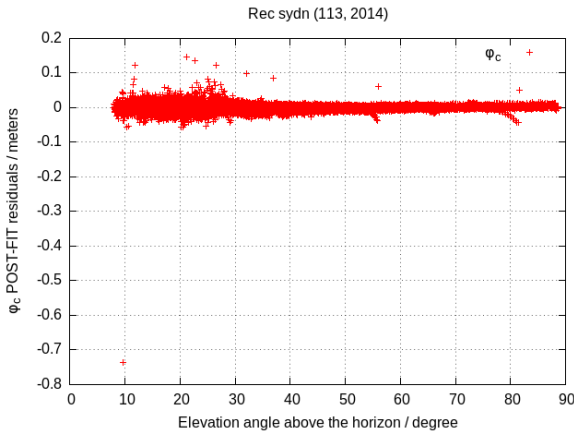
In this section we are commenting how the troposphere delay can be a test for the software performance. Figure 3.2 (a) and (b) are the ZTD estimates with TOMION in red and the IGS final product in blue. In (a) we can notice a discontinuity in the computations around the epoch 28000s and on (c) we can see why. For around 10° of elevation angle, we notice a difference of 70cm between the *pre* and *postfit residuals*. The observations used for this PPP strategy are φ_c and P_c , and hence we compute the residuals for φ_c , because the residuals for the code are not clear due to the measurement noise present in them.



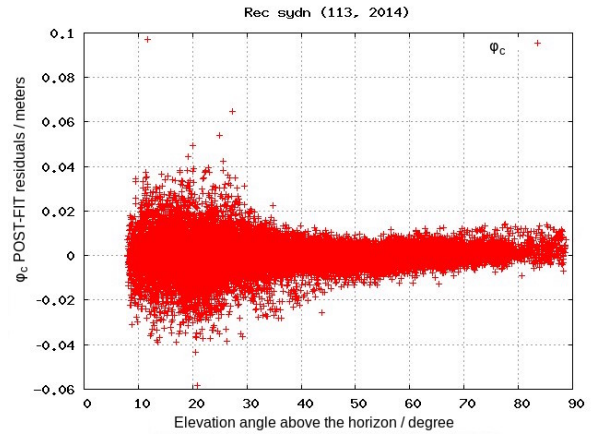
(a) ZTD before filtering the outliers.



(b) ZTD after filtering the outliers.



(c) φ_c Post-fit residuals before filtering the outliers.



(d) φ_c Post-fit residuals after filtering the outliers.

Figure 3.2: The troposphere delay as a quality factor.

Afterwards, in the *postfit* level, this outlier is automatically detected and eliminated as it can be seen on (d) after running the filter again. The result of this second estimation is the ZTD shown in figure (b) where we can see how the discontinuity has been removed.

3.2.3. Filtering the outliers

The graphics in the previous section encouraged us to test how the filter would impact in the rest of the strategies. It was observed that eliminating the observations outliers improved the

estimates in some of the cases while it worsen them in others.

Analyzing figure 3.3 (a) it is clear that while the bias is smaller only for the station *tid1* (5) before eliminating the outliers, the standard deviation curve shown in green for *after* the filter in figure 3.3 (b), goes slightly below the corresponding for the one *before* discarding the outliers. That said, the RMS, that would come to have the final word, shows that the estimates are less different to the IGS product if eliminating the outliers. However, the number of observations would be reduced if this procedure is carried through, except for *tid1*, then it was chosen not to apply this filter because the improvement was not significant. From now on, it was continued to process without removing the outliers until the module is further refined, unless pointed otherwise.

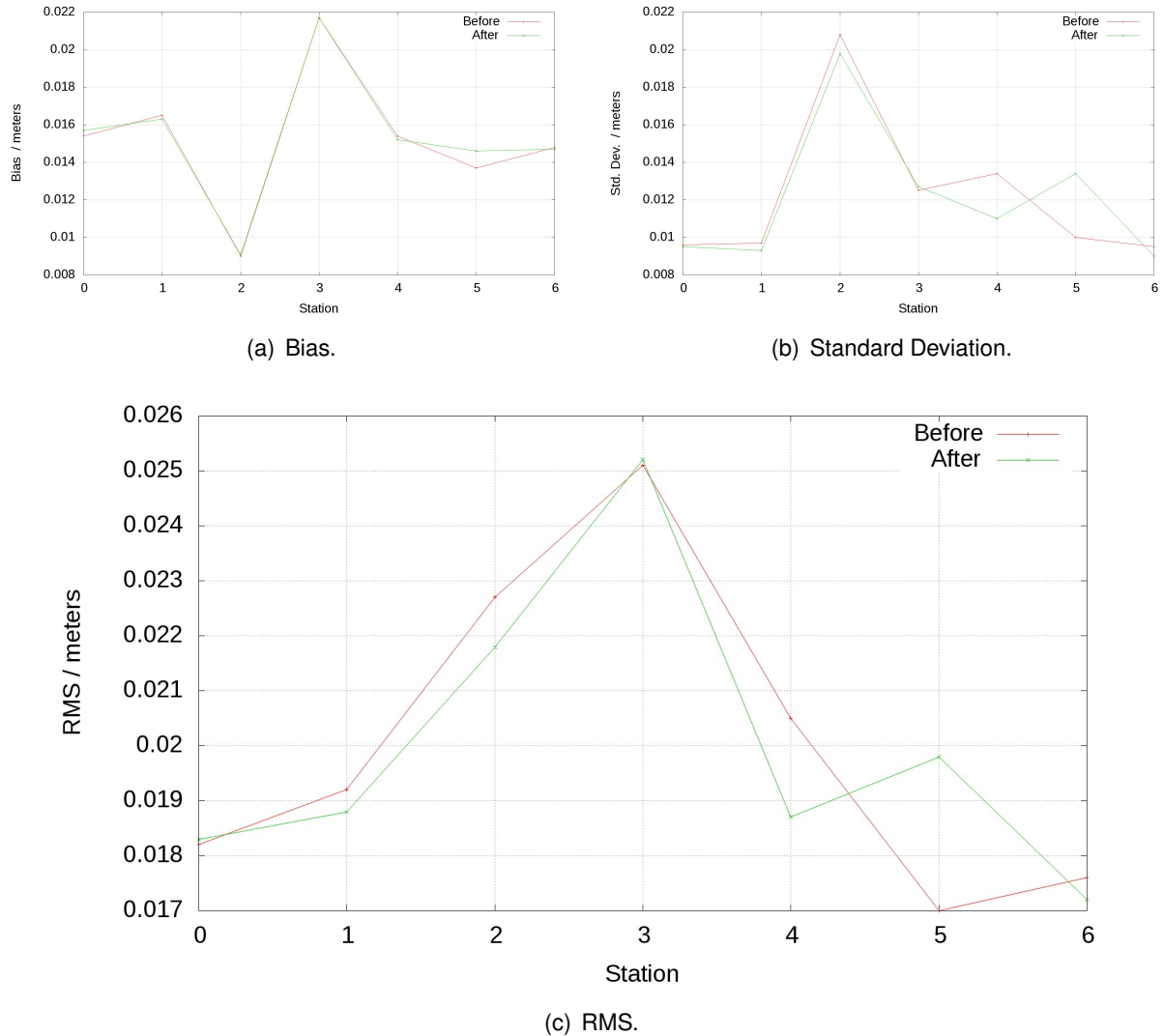


Figure 3.3: Statistics Relative (Niell) w.r.t³ IGS for *before* and *after* removing the outliers.

³w.r.t. stands for *with respect to*

Station	Bias [m]	Std. Dev. [m]	RMS [m]	N° Obs
cedu (0)	0.0154	0.0096	0.0182	254
mobs (1)	0.0165	0.0097	0.0192	254
park (2)	0.0090	0.0208	0.0227	254
str2 (3)	0.0217	0.0125	0.0251	254
sydn (4)	0.0154	0.0134	0.0205	254
tid1 (5)	0.0137	0.0100	0.0170	254
tidb (6)	0.0148	0.0095	0.0176	254

Table 3.1: Statistics WARKT Niell w.r.t. IGS *before* removing filter postfit outliers.

Again, one can notice on table 3.1 and 3.2, the results shown in figure 3.3, corresponding to the bias, the standard deviation and the root mean square of the estimates with respect to IGS products. The number of observation corresponds to one epoch every 5 minutes during the day 113 of the year 2014.

Station	Bias [m]	Std. Dev. [m]	RMS [m]	N° Obs
cedu (0)	0.0157	0.0095	0.0183	254
mobs (1)	0.0163	0.0093	0.0188	254
park (2)	0.0091	0.0198	0.0218	254
str2 (3)	0.0217	0.0127	0.0252	254
sydn (4)	0.0152	0.0110	0.0187	254
tid1 (5)	0.0146	0.0134	0.0198	254
tidb (6)	0.0147	0.0090	0.0172	254

Table 3.2: Statistics WARKT Niell w.r.t. IGS *after* removing filter postfit outliers.

Even though we had found the source of time delay and we have tested the estimates by applying a filter that controls the outliers in the solution of the navigation equations, the bias persisted, showing that the the source of such implications was still to be found. Therefore, we decided to move on to including a new tropospheric mapping function in TOMION.

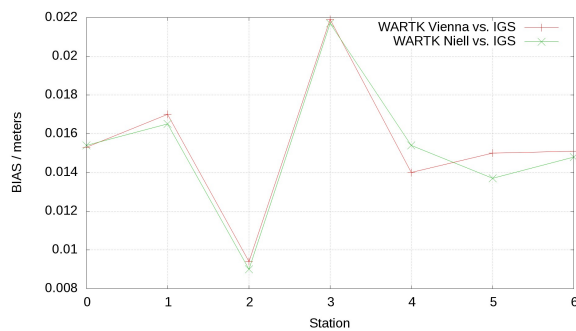
3.3. The new mapping function

The implementation of the Vienna Mapping function was carried out as described in section 2.2.9. and the flow of its functioning can be recalled from figure 2.8. In table 3.3 we can see that for the same scenario as in table 3.1, a difference of about a millimeter is noticed in the bias, standard deviation or rms between the computations with both mapping functions and the IGS products.

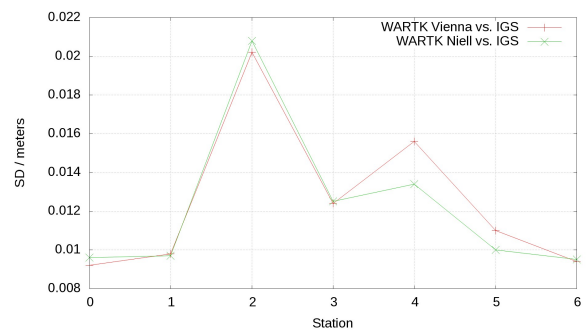
Station	Bias [m]	Std. Dev. [m]	RMS [m]	N° Obs
cedu (0)	0.0153	0.0092	0.0178	254
mobs (1)	0.0170	0.0098	0.0196	254
park (2)	0.0094	0.0202	0.0223	254
str2 (3)	0.0219	0.0124	0.0251	254
sydn (4)	0.0140	0.0156	0.0210	254
tid1 (5)	0.0150	0.0110	0.0186	254
tidb (6)	0.0151	0.0094	0.0178	254

Table 3.3: Statistics WARKT Vienna w.r.t. IGS.

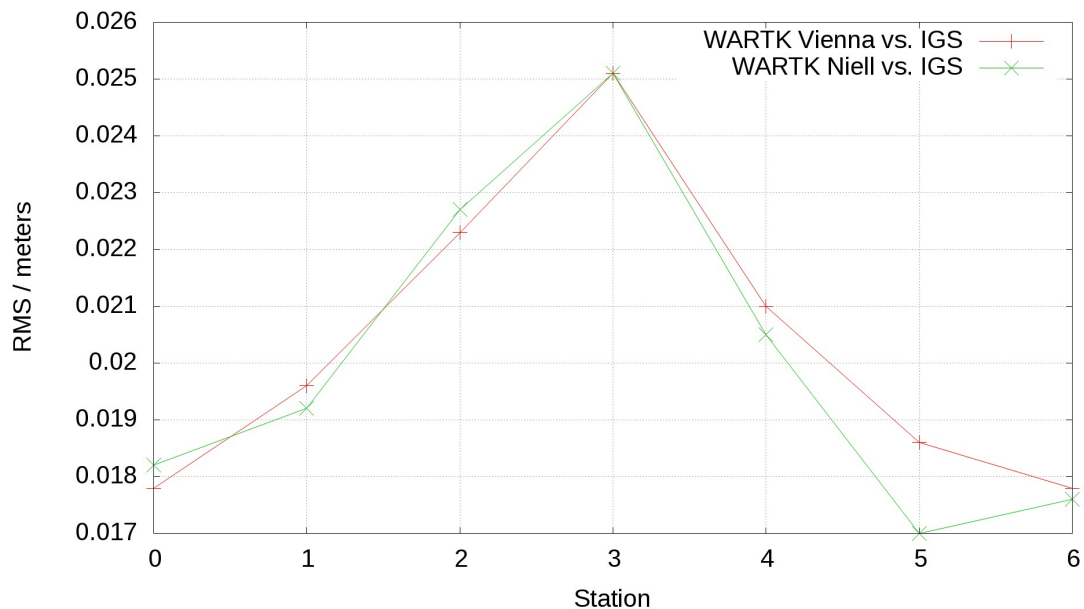
In figure A.3, we can see that while with VMF, the bias is smaller for *sydn* (4), the same statistical value is bigger for *tid1* (5); whereas the standard deviation is smaller for most stations for NMF. The RMS curve for Niell with respect to IGS is below the Vienna one.



(a) Bias.



(b) Standard Deviation.



(c) RMS.

Figure 3.4: Statistics Relative w.r.t IGS for Niell and Vienna mapping functions.

However, this results are in agreement with Steigenberger and Tesmer [2008], where the

authors show that the differences between the Niell and Vienna Mapping functions are only a few millimeters apart, unless for storms conditions or high latitude sites, specially for the southern hemisphere, since the parameters in the NMF were mainly estimated with data from the Northern Hemisphere, hence the performance of VMF should be up to a centimeter better than the NFM one.

It was then discarded that the responsible of the bias between ZTD derived from TOMION and from IGS was the mapping function, hence it was decided to pursue another reference for comparing with the delay. At this point it was settled to integrate GIPSY software as an external call from TOMION script as an option for contrasting TOMION's estimates (see section 2.3.1.). An additional drive for this was to be able to test our ZTD in any cite or epoch, when IGS products are not available, as well as the many parameters that the JPL software estimates.

3.4. Zenith Troposphere Delay

Since TOMION is able to process the observations in multiple modes we decided to examine the performance of WARTK (relative) and PPP (absolute positioning) strategies by the means of the Zenith Total Delay. The reason for selecting these strategies, was that the final objective of the software is to give coordinates and other geodetic parameters in real time, so the strategies were chosen accordingly to such processes even though the tests here were carried out in real time *like mode*.

3.4.1. Relative

Strictly speaking, WARTK would assume a model for the ionosphere [Hernández-Pajares et al., 2004] to be included in the *prefit*, in a synergic way with the geometric modeling. However, for this preliminary study it was not turned on until we have the troposphere refined because introducing such modeling would slow considerably the computations.

For choosing the reference station, the number of observations for each station was studied. As it can be seen on table 3.4, although *mobs* was the one with the greater amount of observations, it was decided that *tibd* was going to be used as reference station for applying the relative positioning principle. The reason for this was the location of *mobs* on the edge of the network, as shown in the map (Fig 2.1). The baselines were computed to support this (see table 3.5).

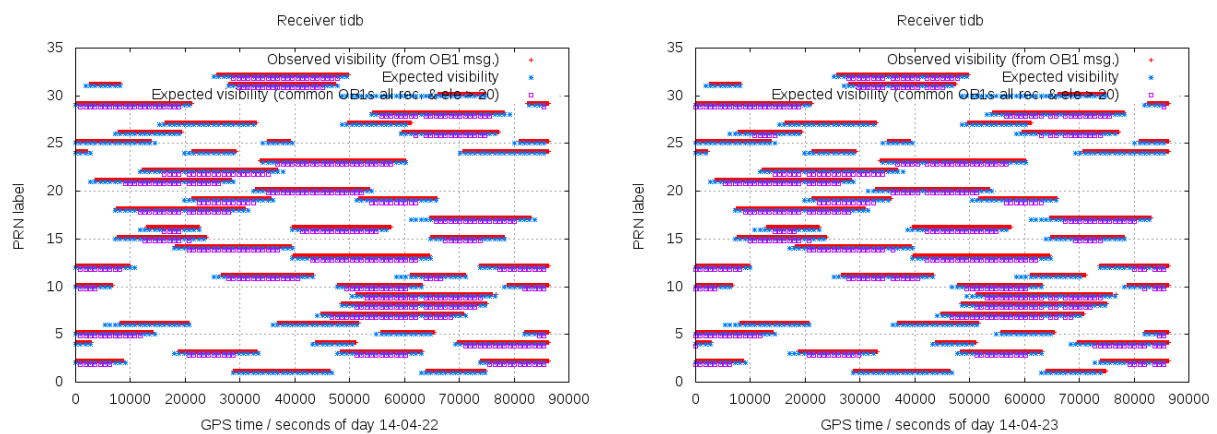
Station	N° Obs
tid1	42029
sydn	47592
str2	48456
park	49034
cedu	49334
tibd	51466
mobs	55053

Table 3.4: Observations for each station for the studied interval.

Station	Distance to ref. rec. [m]
tid1	191847.8757
sydn	268078.1422
str2	9614.5876
park	274312.4220
cedu	1456205.1788
tidb	0.0000
mobs	448267.5558

Table 3.5: Baselines lengths.

Figure 3.5 shows how the reference station tracked all the satellites in view for the studied period of time. And the expected versus the observed visibility is compared. The receiver seems to have enough tracked satellites for this day that is the 113 of 2014.

Figure 3.5: Visibility from reference station *tidb* for both the first (left) and second (right) day of the study.

In figure A.1 we can see the zenith troposphere delay estimated with TOMION in red, the zenith troposphere delay estimated with GIPSY in purple and the IGS final product in blue, for the second day of the study, for two of the stations: *cedu* and *mobs*. We want to remark here that even though the IGS orbits and clocks have been inputs in the TOMION computations, we can clearly see that the agreement of TOMION's estimates with the GIPSY ones is more than a centimeter better, regarding the bias. Leaving aside the high frequency effect of noise we still have to diminish, the systematic larger estimation appears to be mitigated.

We should note that both graphics included are for the longer baselines computed in relative mode, as it can be noted in table 3.5.

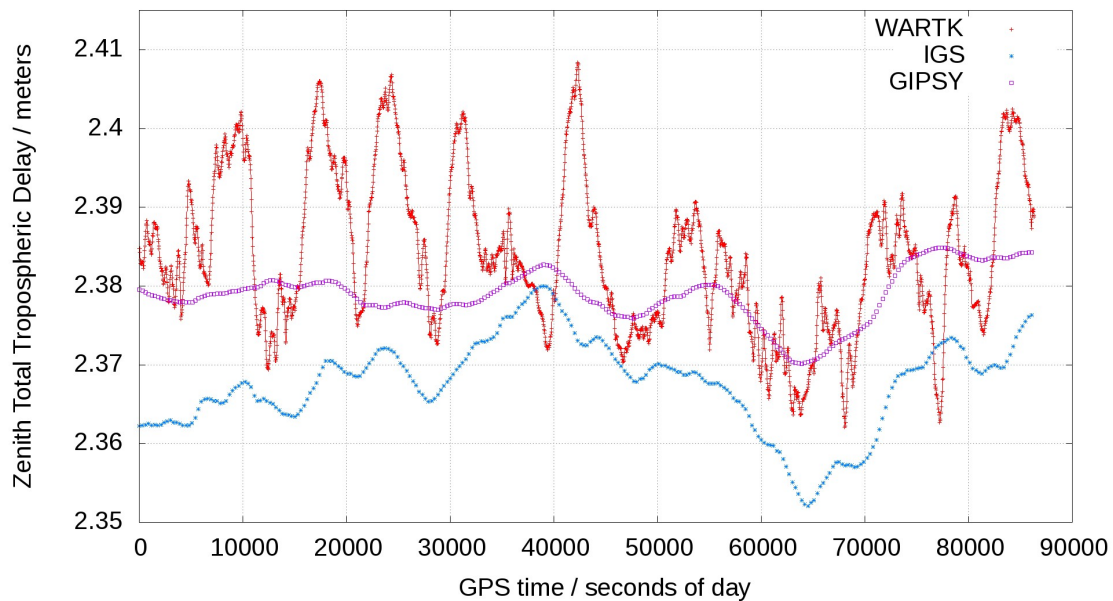
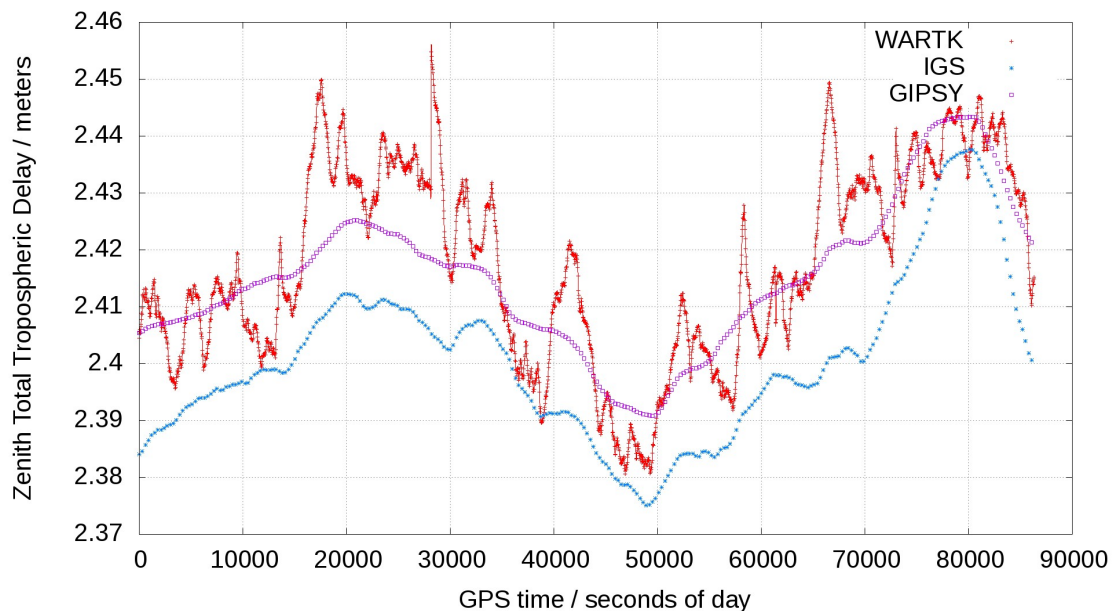
(a) ZTD for *cedu*, day 113 of 2014.(b) ZTD for *mobs*, day 113 of 2014.

Figure 3.6: ZTD computed in WARTK (Vienna) mode with TOMION (red), with GIPSY (purple) and IGS final product (blue).

The results above were performed using the Vienna mapping function and for completeness, the ZTD was also computed with the NMF and compared with GIPSY as well. We do not show the plots here, they are in the appendix ??, but we show the statistics related to them.

In figure 3.7 we can see the comparison between the ZTD derived from TOMION estimated with NMF and with VMF with respect to GIPSY. We should point out that the bias is in the neighborhood of the zero value plus minus 5mm, which means an improvement of the agreement in bias of over 1.5 cm with respect to IGS, for both mapping functions. The estimates done with NMF appear less of a millimeter below the ones for VMF. This represents less than 0.1% of a

typical value of a delay, of about 2.4 meters. Therefore this difference in practice is inexistent.

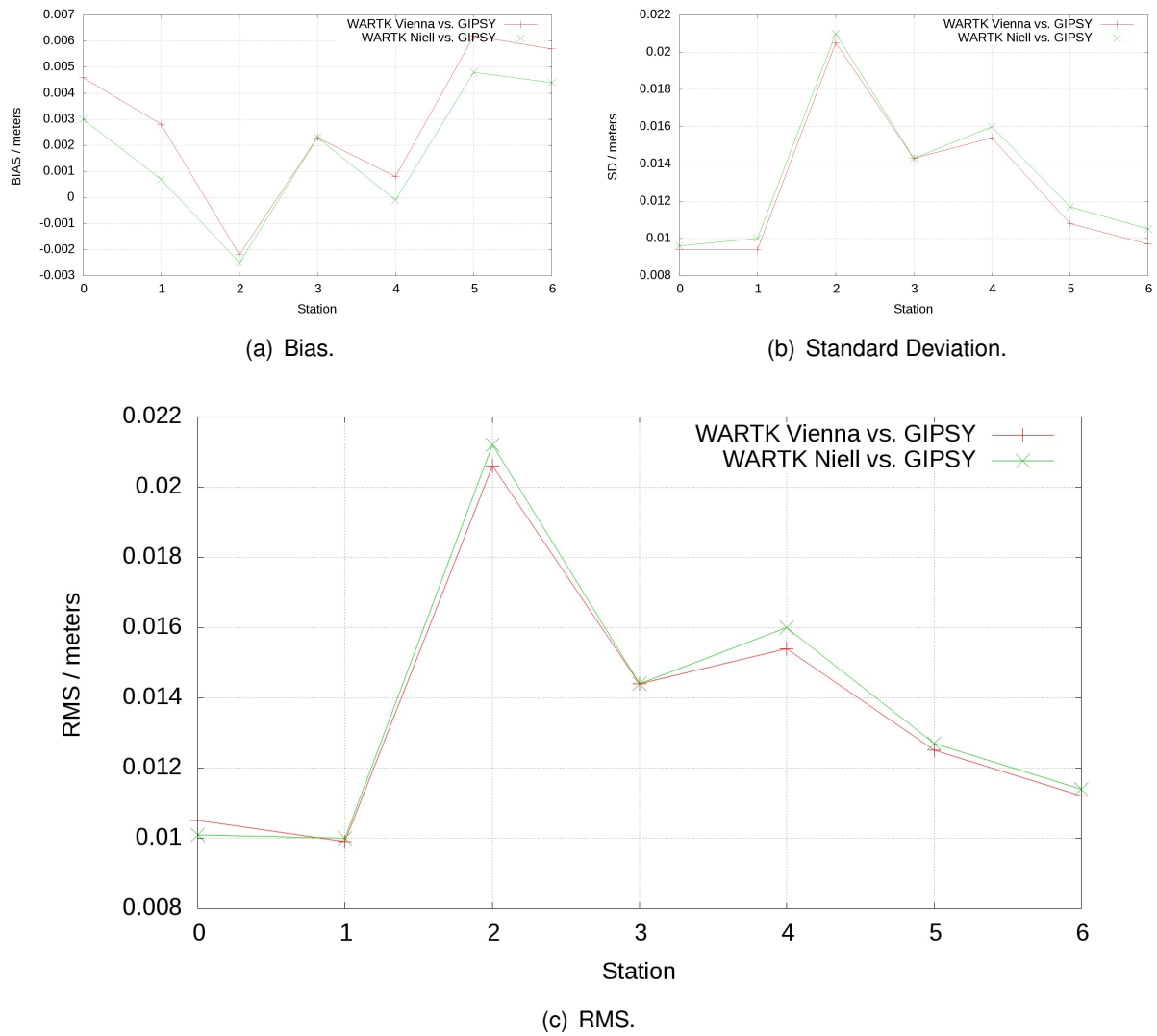


Figure 3.7: Statistics Relative w.r.t GIPSY for Niell and Vienna mapping functions.

Station	Bias [m]	Std. Dev. [m]	RMS [m]	N° Obs
cedu (0)	0.0030	0.0096	0.0101	254
mobs (1)	0.0007	0.0100	0.0100	254
park (2)	-0.0025	0.0210	0.0212	247
str2 (3)	0.0023	0.0143	0.0144	254
sydn (4)	-0.0001	0.0160	0.0160	254
tid1 (5)	0.0048	0.0117	0.0127	254
tidb (6)	0.0044	0.0105	0.0114	254

Table 3.6: Statistics WARKT Niell w.r.t GIPSY.

The comparatives in tables 3.6 and 3.7 show a bias of less than one centimeter for all stations and both mapping functions when contrasted with GIPSY estimates, when for the comparatives with IGS they were about 2 cm. The RMS and the standard deviation does not seem

to improve much with respect to this second reference. VMF seems to behave slightly fitter for this strategy than NFM, although the difference with the estimates with Niell is less than 1 mm in the worst cases for the bias, as mentioned before.

Station	Bias [m]	Std. Dev. [m]	RMS [m]	N° Obs
cedu (0)	0.0046	0.0094	0.0105	254
mobs (1)	0.0028	0.0094	0.0099	254
park (2)	-0.0022	0.0205	0.0206	247
str2 (3)	0.0023	0.0143	0.0144	254
sydn (4)	0.0008	0.0154	0.0154	254
tid1 (5)	0.0062	0.0108	0.0125	254
tidb (6)	0.0057	0.0097	0.0112	254

Table 3.7: Statistics WARKT Vienna w.r.t GIPSY.

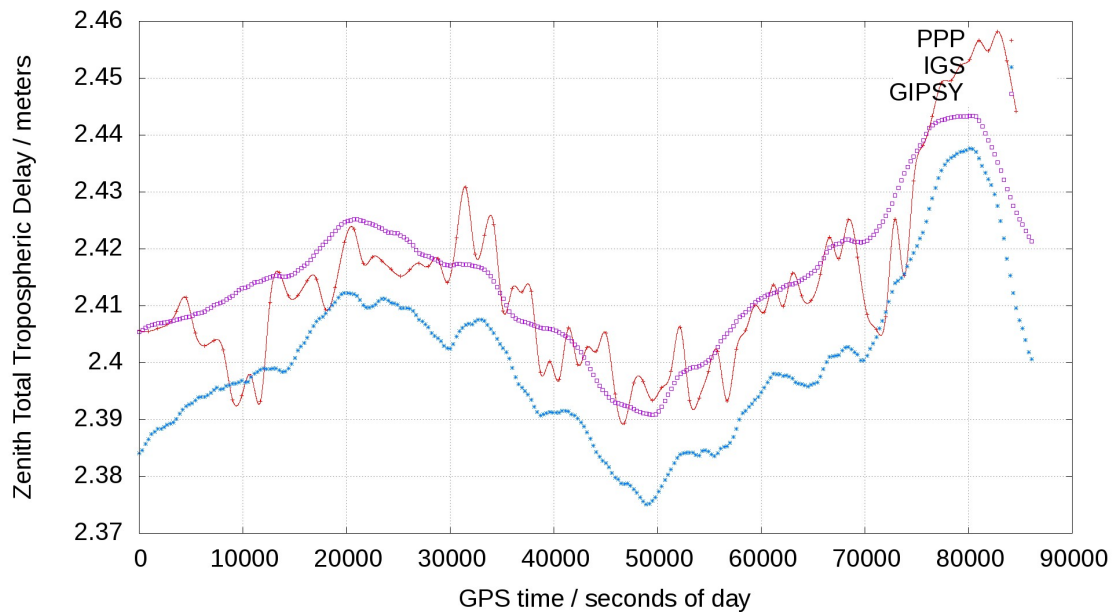
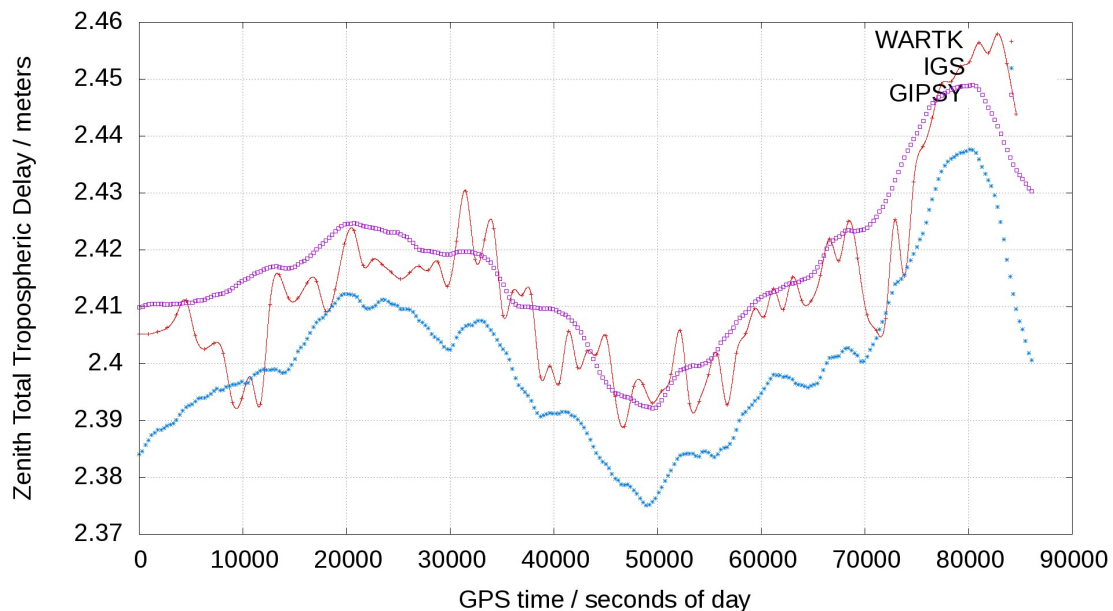
3.4.2. PPP

To further improve the estimates and test the software we have also process the same set of data with Precise Point Positioning (PPP) strategy, already implemented as an option in the TOMION software. Again, for completeness we have computed for both mapping functions and with respect to both references, which lead to 4 new sets of ZTDs and its comparisons. But we have only included relevant plots in the main text while the rest are in the appendix ??

In figure 3.8 we can see the zenith troposphere delay estimated with TOMION, the zenith troposphere delay estimated with GIPSY and the IGS final product. Again, the agreement is better with GIPSY estimates, despite we have continued using IGS orbits and clocks. The bias is persistent with what was observed for WARTK mode: of about 2 cm with respect to IGS and of a few millimeters with respect to GIPSY. Although the high frequency noise has not been mitigated, the software calculations follows the long periods variations and appears to be in phase with the reference.

Furthermore, the results are presented for VMF in (a) and for NMF in (b). The curves in red corresponding to TOMION estimates resemble and there seems to be negligible difference between them. These cases will be deeper examined once the software is more stable for sensitive parameters such as the ZTD.

Note that the points have been connected by a polynomial of third degree for a better visualization of the results, since there is only one estimated value every 15 minutes because the procedure is done in PPP strategy but in real time *like* mode, which means no post processing has been done. As a consequence, since the IGS satellite clock offsets corrections are only available every 900 seconds (and the orbits but it is not a major inconvenience, because they are easily interpolated), and are highly unpredictable, the estimation has only been done in those epochs.

(a) ZTD for *mobs*, day 113 of 2014.(b) ZTD for *mobs*, day 113 of 2014.Figure 3.8: Zenith Troposphere Delay in PPP mode for receiver *mobs*; (a) for Vienna and (b) for Niell.

In figure 3.9 shows the performance of both mapping functions in PPP mode now. Although the bias seems to be smaller for NMF, the standard deviation improves slightly for VMF; but if we compare with the statistics for the WARTK mode (fig 3.7), the values of the standard deviation are considerably reduced in PPP mode, about 1 centimeter less, while the bias was nearly the same for both strategies, always with respect to GIPSY. The RMS tends to follow the greater values of the other two, so it resembles the standard deviation and as a consequence is also 1 centimeter smaller for PPP than for WARKT.

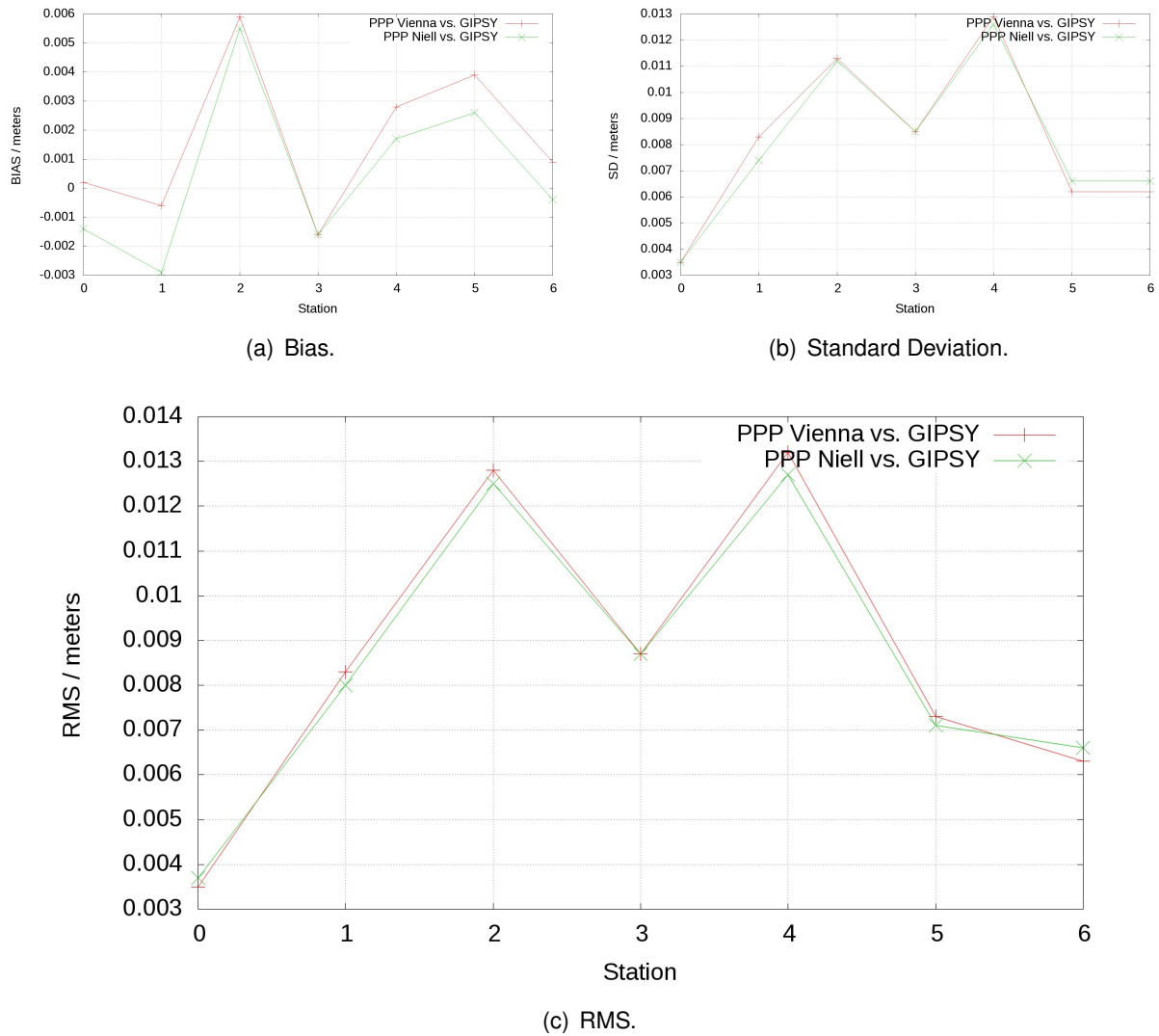


Figure 3.9: Statistics PPP w.r.t. GIPSY for Niell and Vienna mapping functions.

Station	bias	stad. dev.	RMS	N° Obs
cedu (1)	0.0002	0.0035	0.0035	83
mobs (2)	-0.0006	0.0083	0.0083	83
park (3)	0.0059	0.0113	0.0128	80
str2 (4)	-0.0016	0.0085	0.0087	83
sydn (5)	0.0028	0.0129	0.0132	78
tid1 (6)	0.0039	0.0062	0.0073	83
tidb (7)	0.0009	0.0062	0.0063	83

Table 3.8: Statistics PPP Vienna w.r.t. GIPSY

The comparatives in tables 3.9 and 3.8 present the numerical values plotted in figure 3.9 and denote the smaller numbers in general with respect to tables 3.6 and 3.7, as it was mentioned above. This reinforces the fact that the estimates approached with PPP strategy are similarly biased but less deviated than if approached with WARTK. Also, note that there are 83

observations for each site, which corresponds to one epoch every 15 unites, except for *sydn* and *park* where there might have been GPS signal loss.

Station	bias	stad. dev.	RMS	N° Obs
cedu (1)	-0.0014	0.0035	0.0037	83
mobs (2)	-0.0029	0.0074	0.0080	83
park (3)	0.0055	0.0112	0.0125	80
str2 (3)	-0.0016	0.0085	0.0087	83
sydn (4)	0.0017	0.0126	0.0127	78
tid1 (5)	0.0026	0.0066	0.0071	83
tidb (6)	-0.0004	0.0066	0.0066	83

Table 3.9: Statistics PPP Niell w.r.t. GIPSY

3.5. Summary of results

Figures 3.10, 3.11 and 3.12 show the bias, standard deviation and the root mean square of the zenith tropospheric delay estimated with TOMION with respect to the references: IGS and GIPSY, respectively.

Firstly, as we have commented above, focusing on figure 3.10, we can notice that the agreement with the GIPSY estimates are nearly unbiased while the respective with IGS product are systematically above one centimeter the IGS values for all the strategies, since all 4 curves corresponding to comparatives with respect to IGS are bounded between one and 2.2 cm approximately. In addition, although for PPP strategy there seems to be a deficiency for station *mobs* (2), the other dots corresponding to this absolute mode hardly move apart from the zero mean. In contrast, the bias for WARTK seems to oscillate more for the other sites, however the maximum value was of about 6 millimeters.

On the other hand, now looking at figure 3.11, the smaller standard deviations correspond to the 4 curves of PPP mode, even for comparatives with respect to IGS. All the plots above 1cm of SD come from WARTK mode. Hence, there is a considerably improvement on hands of the absolute technique regarding the relative, but it should be reminded here that the approach is daring because of the length of some of the baselines and *only* considering forward processing, because of the simulation of real time processing.

Finally, the RMS curves, plotted on figure 3.12, that would put together the SD and Bias results, show that the best two curves are for estimates in PPP processing mode with respect to GIPSY estimates, for both mapping functions. In spite of having the higher SD, the WARTK technique shows RMS between 1 and 2 cm w.r.t GIPSY while the 4 curves plotting greater values out of the total 8 sets, come from comparisons with IGS.

Certainly, the smaller standard deviation in the PPP technique together with the bias centered in zero, make this approach the most interesting one in TOMION and when it comes to Zenith Troposphere Delay estimations.

Both mapping functions seem to project the troposphere slant delay in a very similar way except for a slight improvement in the bias on the hands of VMF. For the root mean square and the standard deviation, the difference is unnoticeable. In WARTK mode, NMF seems to have

smaller SD than VMF. For PPP the difference looks imperceptible.

Even though there seems to be no significant difference between the estimation with one or the other mapping function, we do not discard that once the software is further refined in sections such as ambiguity fixing or very small cycle slip detection, then VMF would make a finer performance than NFM. And we expect to exploit this feature in the near future. For now the differences between them appear below values of noise, high in some cases.

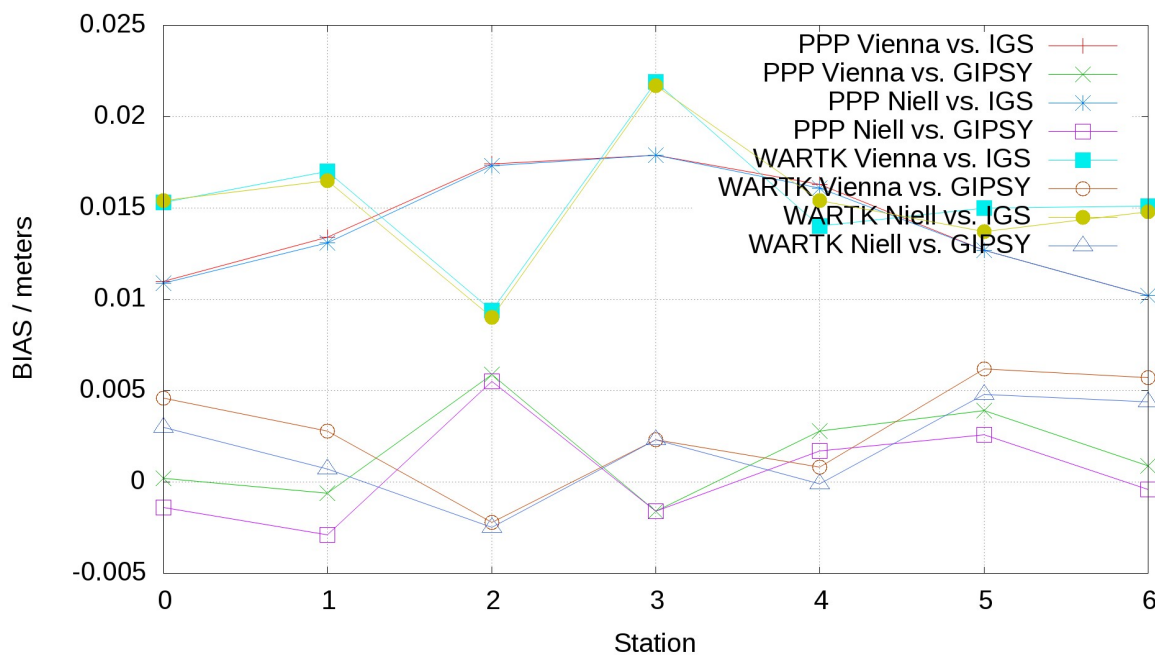


Figure 3.10: BIAS of ZTD in PPP and in WARTK strategies, for Niell and Vienna mapping functions w.r.t GIPSY and IGS.

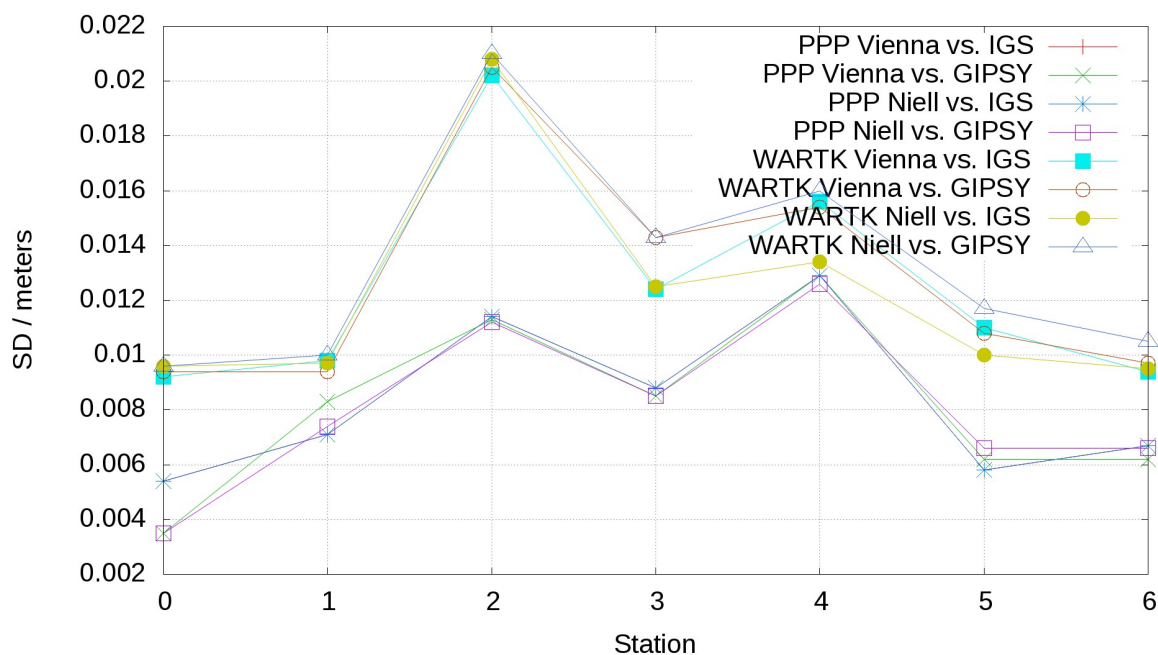


Figure 3.11: SD of ZTD in PPP and in WARTK strategies, for Niell and Vienna mapping functions w.r.t GIPSY and IGS.

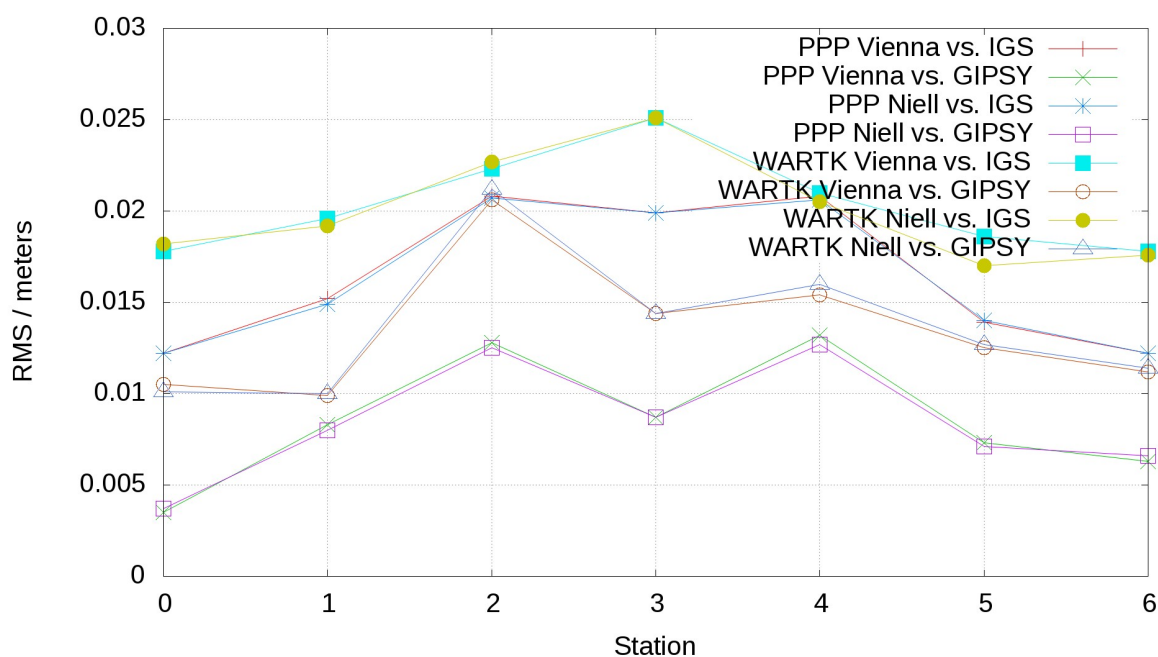


Figure 3.12: of ZTD in PPP and in WARTK strategies, for Niell and Vienna mapping functions w.r.t GIPSY and IGS.

CONCLUSIONS

With the geodetic and ionospheric software, TOMographic Model of the IONospheric electron content (TOMION), real-time zenith tropospheric total delays (ZTD) can be typically computed every 30 seconds in relative mode and every 15 minutes in absolute mode.

In a comparative analysis, it is shown that the agreement of TOMION estimates emulating real time, with respect to IGS products is typically of 2cm. However, zenith tropospheric delays from an external software (GIPSY/OASIS) were contrasted as well, resulting in a reduction to 5mm of bias. This quantity represents less than 0.1% of a typical value for the ZTD of about 2.3m while for the comparison with the IGS products the difference represents 1% of the total delay, even though for TOMION's computations, IGS clocks and orbits were introduced.

For the strategies exploited, Precise Point Positioning seemed to be the most accurate one regarding the closest reference improving from 2 to 1 cm the standard deviation when compared to WARTK. Although, the conditions for kinematic relative positioning were not the optimal ones here, since no ionospheric model was applied and it would be recommended for such a large area.

The new mapping function, Vienna mapping function (VMF1) was contrasted with the already functional in the software, Niell mapping function and it could be said that both seem to project the troposphere slant delay equivalently except for a slight improvement in the bias upon VMF1, but still, further investigations remain to be done.

Future works

We are expecting to test in the near future the potential improvements given by the introduction of a model for the ionosphere, which is presently one of the novel features on TOMION. We will focus on the trade off retrieval between time consuming and improvement of the estimates.

On the other hand for validating the zenith tropospheric delay it is hoped to obtain radiosonde data for the locations involved in this study. Also, we will test if it is possible to use the plane receiver as a sonde for the troposphere, that is for the plane trajectory.

Furthermore, it is intended to continue refining the troposphere mapping function with ray-traced coefficients for the IGS sites, and an alternative for not relying on streamed data will be further pursued.

BIBLIOGRAPHY

- Askne, J. and Nordius, H. (1987). Estimation of tropospheric delay for microwaves from surface weather data. *Radio Science*, 22(3):379–386. 3, 29
- Bernhard Hofmann-Wellenhof, H. L. and Wasle, E. (2008). *GNSS - Global Navigation Satellite Systems*. Springer. 14
- Boehm, J. and Schuh, H. (2004). Vienna mapping functions in vlbi analyses. *Geophysical Research Letters*, 31(1). 4, 5, 7
- Böhm, J., Möller, G., Schindelegger, M., Pain, G., and Weber, R. (2015). Development of an improved empirical model for slant delays in the troposphere (gpt2w). *GPS Solutions*, 19(3):433–441. 8, 9, 28
- Böhm, J., Niell, A., Tregoning, P., and Schuh, H. (2006). Global mapping function (gmf): A new empirical mapping function based on numerical weather model data. *Geophysical Research Letters*, 33(7). 4, 7, 8
- Böhm, J. and Schuh, H. (2013). *Atmospheric effects in space geodesy*. Springer. 5
- Colombo, O. L. (2006). A zenith delay model for precise kinematic aircraft navigation. In *Proceedings of ION GNSS 19th International Technical Meeting of the Satellite Division, Fort Worth, US*, pages 68–76. 11
- Davis, J., Herring, T., Shapiro, I., Rogers, A., and Elgered, G. (1985). Geodesy by radio interferometry: Effects of atmospheric modeling errors on estimates of baseline length. *Radio science*, 20(6):1593–1607. 2, 3, 4
- García-Fernández, M., Hernandez-Pajares, M., Juan, J., Sanz, J., Orus, R., Coisson, P., Nava, B., and Radicella, S. (2003). Combining ionosonde with ground gps data for electron density estimation. *Journal of atmospheric and solar-terrestrial physics*, 65(6):683–691. 12
- GGOS (2017). Global geodetic observing system, <http://ggosatm.hg.tuwien.ac.at/>. 8, 29, 31
- Graffigna, V., Gende, M., Hernández-Pajares, M., and García-Rigo, A. (2017a). Validación del retardo troposférico cenital y evolución de las funciones de mapeo en tomion. In *Argentine Geodesy and Geophysics Association meeting, La Plata, Argentina*. 1
- Graffigna, V., Hernández-Pajares, M., and García-Rigo, A. (2016). Assessing different components of the real-time gnss precise positioning "sudoku" with tomion software. In *Workshop on Space Geodesy and Ionospheric Research (SGI) , Berlin, Germany*. 1
- Graffigna, V., Hernández-Pajares, M., García-Rigo, A., and Gende, M. (2017b). Consistency of different tropospheric models and mapping functions for precise gnss processing. In *European Geosciences Union General Assembly 2017, Vienna, Austria*. 1
- Haase, J., Ge, M., Vedel, H., and Calais, E. (2003). Accuracy and variability of gps tropospheric delay measurements of water vapor in the western mediterranean. *Journal of Applied Meteorology*, 42(11):1547–1568. 34

- Hernández-Pajares, M., Juan, J., and Sanz, J. (2000a). Improving the abel inversion by adding ground gps data to leo radio occultations in ionospheric sounding. *Geophysical Research Letters*, 27(16):2473–2476. 12
- Hernández-Pajares, M., Juan, J., Sanz, J., and Colombo, O. (2002). Improving the real-time ionospheric determination from gps sites at very long distances over the equator. *Journal of Geophysical Research: Space Physics*, 107(A10). 12
- Hernández-Pajares, M., Juan, J., Sanz, J., Colombo, O., and Van der Marel, H. (2000b). Real-time integrated water vapor determination using otf carrier-phase ambiguity resolution in wadgps networks. In *ION GPS*. 12, 28
- Hernández-Pajares, M., Juan, J., Sanz, J., and Colombo, O. L. (2000c). Application of ionospheric tomography to real-time gps carrier-phase ambiguities resolution, at scales of 400–1000 km and with high geomagnetic activity. *Geophysical Research Letters*, 27(13):2009–2012. 12, 27
- Hernández-Pajares, M., Juan, J., Sanz, J., Orus, R., Garcia-Rigo, A., Feltens, J., Komjathy, A., Schaer, S., and Krankowski, A. (2009). The igs vtec maps: a reliable source of ionospheric information since 1998. *Journal of Geodesy*, 83(3-4):263–275. 12
- Hernández-Pajares, M., Juan, J., Sanz, J., and Sole, J. (1998). Global observation of the ionospheric electronic response to solar events using ground and leo gps data. *Journal of Geophysical Research: Space Physics*, 103(A9):20789–20796. 12
- Hernández-Pajares, M., Juan, J. M., Sanz, J., Orús, R., García-Rodríguez, A., and Colombo, O. L. (2004). Wide area real time kinematics with galileo and gps signals. *Europe*, 17:03–00. 25, 39
- Herring, T. (1992). Modeling atmospheric delays in the analysis of space geodetic data. *Proceedings of Refraction of Transatmospheric signals in Geodesy*, eds. JC De Munck and TA Spoelstra, Netherlands Geodetic Commission Publications on Geodesy, 36. 4
- IGS (2017). International gnss service, <http://www.igs.org/>. 32
- Kleusberg, A. and Teunissen, P. J. G. (1996). *GPS for Geodesy*, volume 60. Springer. 14
- Lagler, K., Schindelegger, M., Böhm, J., Krásná, H., and Nilsson, T. (2013). Gpt2: Empirical slant delay model for radio space geodetic techniques. *Geophysical research letters*, 40(6):1069–1073. 8
- Marini, J. W. (1972). Correction of satellite tracking data for an arbitrary tropospheric profile. *Radio Science*, 7(2):223–231. 4
- Niell, A. (1996). Global mapping functions for the atmosphere delay at radio wavelengths. *Journal of Geophysical Research: Solid Earth*, 101(B2):3227–3246. 4, 28
- Niell, A. (2000). Improved atmospheric mapping functions for vlbi and gps. *Earth, planets and space*, 52(10):699–702. 4
- Saastamoinen, J. (1972). Atmospheric correction for the troposphere and stratosphere in radio ranging satellites. *The use of artificial satellites for geodesy*, pages 247–251. 2

- Sanz, J., Juan, J., and Hernández-Pajares, M. (2013). Gns data processing, vol. i: Fundamentals and algorithms. *ESA Communications*. 14, 15
- Steigenberger, P. and Tesmer, V. (2008). Impact of different troposphere modeling on gps-and vlbi-derived parameters. *Journal of Applied Meteorology*, 42(11):1547–1568. 38
- Thayer, G. D. (1974). An improved equation for the radio refractive index of air. *Radio Science*, 9(10):803–807. 3
- Van der Marel, H., Verhagen, S., De Bakker, P., Teunissen, P. J., Odijk, D., Hernández Pajares, M., Zornoza, J., Miguel, J., Sanz Subirana, J., Ángel, A., et al. (2010). Wide-area rtk: high precision positioning on a continental scale. *Inside GNSS*, 5(2):35–46. 12
- Zumberge, J., Heflin, M., Jefferson, D., Watkins, M., and Webb, F. H. (1997). Precise point positioning for the efficient and robust analysis of gps data from large networks. *Journal of Geophysical Research: Solid Earth*, 102(B3):5005–5017. 22, 31, 33

APPENDICES

Appendix A

Appendix

A.1. Coefficients for Niell Mapping Function

coefficient	Latitude (deg)				
	15°	30°	45°	60°	75°
	average				
a	1.2769934e-3	1.2683230e-3	1.2465397e-3	1.2196049e-3	1.2045996e-3
b	2.9153695e-3	2.9152299e-3	2.9288445e-3	2.9022565e-3	2.9024912e-3
c	62.610505e-3	62.837393e-3	63.721774e-3	63.824265e-3	64.258455e-3
	amplitude				
a	0.0	1.2709626e-5	2.6523662e-5	3.4000452e-5	4.1202191e-5
b	0.0	2.1414979e-5	3.0160779e-5	7.2562722e-5	11.723375e-5
c	0.0	9.0128400e-5	4.3497037e-5	84.795348e-5	170.37206e-5
	height correction				
		a_{ht}	2.53e-5		
		b_{ht}	5.49e-3		
		c_{ht}	1.14e-3		

Table A.1: Coefficients of the Niell hydrostatic mapping function.

coefficient	Latitude (deg)				
	15°	30°	45°	60°	75°
a	5.8021897e-4	5.6794847e-4	5.8118019e-4	5.9727542e-4	6.1641693e-4
b	1.4275268e-3	1.5138625e-3	1.4572752e-3	1.5007428e-3	1.7599082e-3
c	4.3472961e-2	4.6729510e-2	4.3908931e-2	4.4626982e-2	5.4736038e-2

Table A.2: Coefficients of the Niell wet mapping function.

A.2. Combinations of measurements

Starting from the basic observables as described in section 2.2.3., the following combinations can be defined:

Ionosphere-free combination:

This removes the first-order (up to 99.9%) ionospheric effect, which depends on the inverse

square of the frequency ($\alpha_i \propto \frac{1}{f_i^2}$):

$$\varphi_c = \frac{f_1^2 \varphi_1 - f_2^2 \varphi_2}{f_1^2 - f_2^2}, \quad R_c = \frac{f_1^2 R_1 - f_2^2 R_2}{f_1^2 - f_2^2}. \quad (\text{A.1})$$

Geometry-free (or ionospheric) combination:

This cancels the geometric part of the measurement, leaving all the frequency-dependent effects (i.e. ionospheric refraction, instrumental delays, wind-up). It can be used to estimate the ionospheric electron content or to detect cycle slips in the carrier phase, as well. Note the change in the order of terms in φ_I and R_I

$$\varphi_I = \varphi_1 - \varphi_2, \quad R_I = R_2 - R_1. \quad (\text{A.2})$$

Wide-laning combinations:

These combinations are used to create a measurement with a significantly wide wavelength. This longer wavelength is useful for carrier phase cycle-slip detection and fixing ambiguities:

$$\varphi_W = \frac{f_1 \varphi_1 - f_2 \varphi_2}{f_1 - f_2}, \quad R_W = \frac{f_1 R_1 - f_2 R_2}{f_1 - f_2}. \quad (\text{A.3})$$

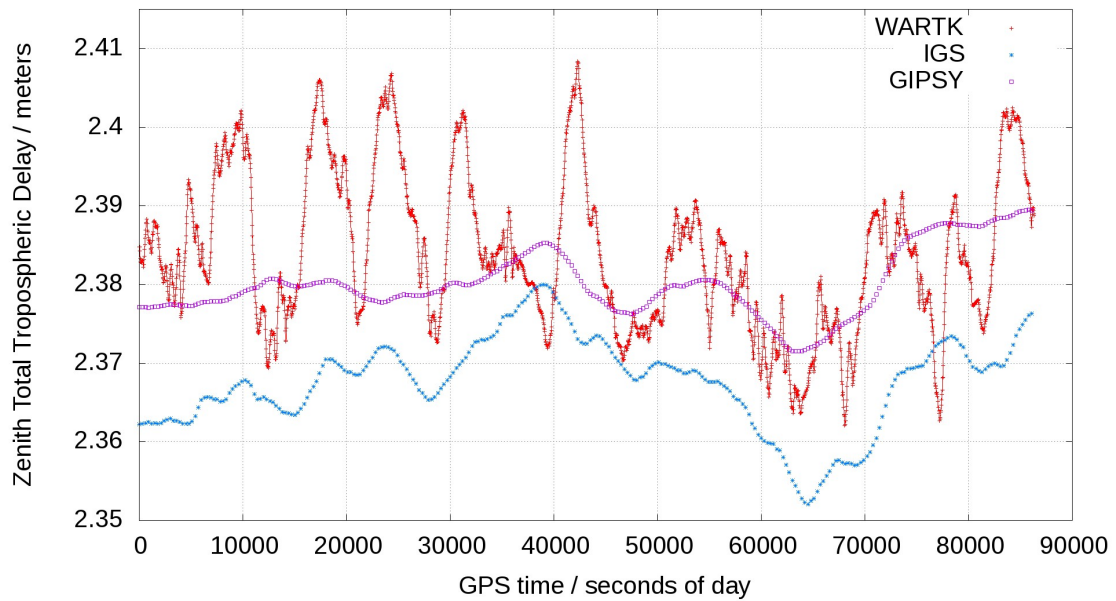
Narrow-laning combinations:

These combinations create measurements with a narrow wavelength. The measurement in this combination has a lower noise than each separate component:

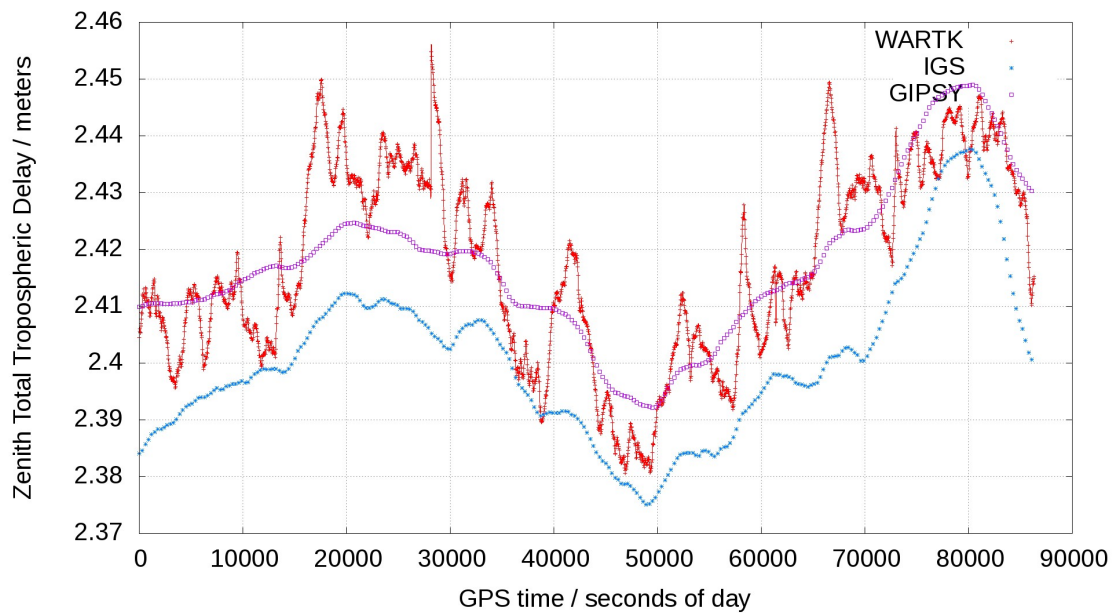
$$\varphi_n = \frac{f_1 \varphi_1 + f_2 \varphi_2}{f_1 + f_2}, \quad R_n = \frac{f_1 R_1 + f_2 R_2}{f_1 + f_2}. \quad (\text{A.4})$$

where φ_n and R_n have the same ionospheric dependence, which is exploited by the Melbourne-Wübbena combination to remove the ionospheric refraction, as it was explained in section 2.2.8..

A.3. Zenith Tropospheric Delay in WARTK mode for Niell Mapping Function



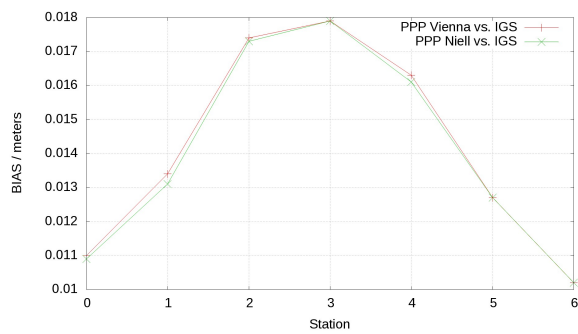
(a) ZTD for *cedu*, day 113 of 2014.



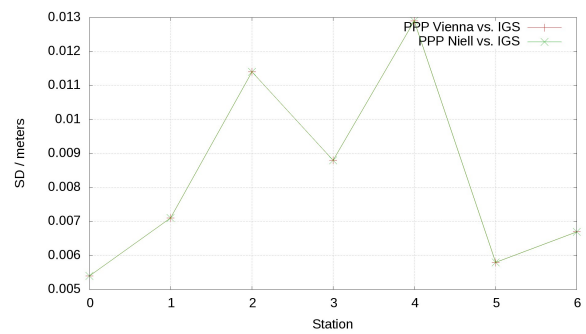
(b) ZTD for *mobs*, day 113 of 2014.

Figure A.1: ZTD computed in WARTK (Niell) mode with TOMION (red), with GIPSY (purple) and IGS final product (blue).

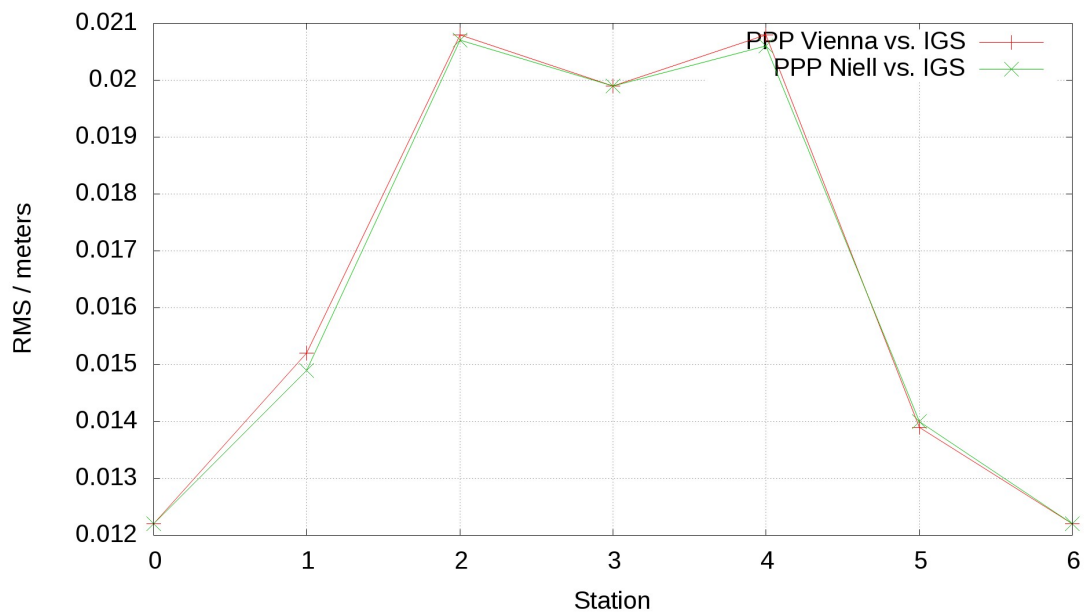
A.4. Statistics of the comparison between the mapping functions in Precise Point Positioning



(a) Bias.

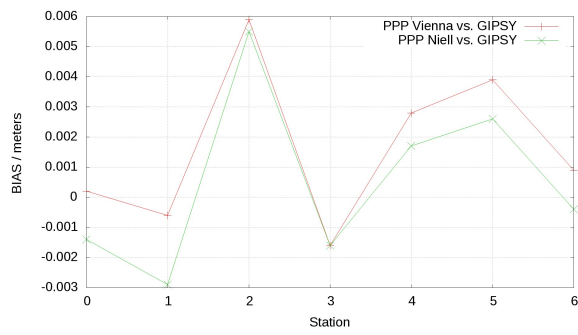


(b) Standard Deviation.

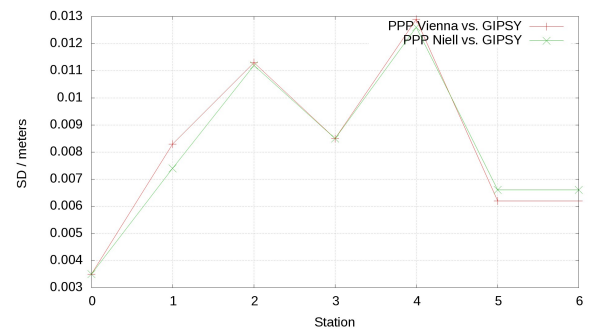


(c) RMS.

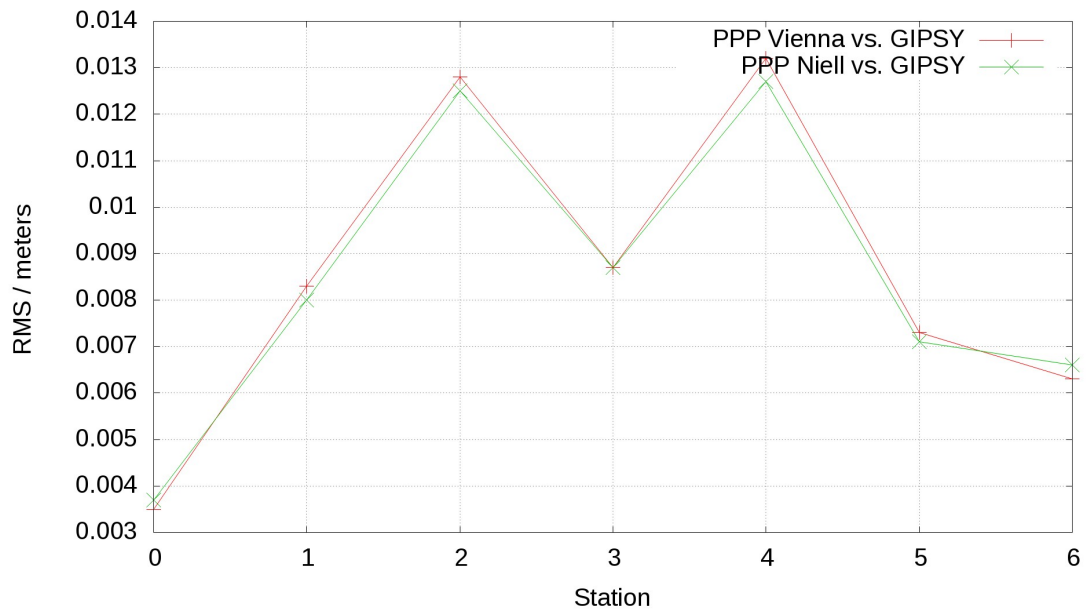
Figure A.2: Statistics PPP w.r.t IGS for Niell and Vienna mapping functions.



(a) Bias.



(b) Standard Deviation.



(c) RMS.

Figure A.3: Statistics PPP w.r.t GIPSY for Niell and Vienna mapping functions.